AD-A130 630

AD A 130 630

TECHNICAL
LIBRARY

AD

TECHNICAL REPORT ARBRL-TR-02501

NAVIER-STOKES COMPUTATIONAL STUDY OF THE INFLUENCE OF SHELL GEOMETRY ON THE MAGNUS EFFECT AT SUPERSONIC SPEEDS

Walter B. Sturek
Donald C. Mylin
Bernard Guidos
Charles J. Nietubicz

June 1983

US ARMY ARMAMENT RESEARCH AND DEVELOPMENT COMMAND
BALLISTIC RESEARCH LABORATORY
ABERDEEN PROVING GROUND, MARYLAND

Approved for public release; distribution unlimited.

Destroy this report when it is no longer needed.
Do not return it to the originator.

Additional copies of this report may be obtained from the National Technical Information Service, U. S. Department of Commerce, Springfield, Virginia 22161.

The findings in this report are not to be construed as an official Department of the Army position, unless so designated by other authorized documents.

The use of trade names or manufacturers' names in this report does not constitute indorsement of any commercial product.

UNCLASSIFIED

SECURITY CLASSIFICATION OF THIS PAGE (When Data Entered)

REPORT DOCUMENTATION PAGE

READ INSTRUCTIONS BEFORE COMPLETING FORM

1. REPORT NUMBER
TECHNICAL REPORT ARBRL-TR-02501

2. GOVT ACCESSION NO.

3. RECIPIENT'S CATALOG NUMBER

4. TITLE (and Subtitle)
NAVIER-STOKES COMPUTATIONAL STUDY OF THE INFLUENCE OF SHELL GEOMETRY ON THE MAGNUS EFFECT AT SUPERSONIC SPEEDS

5. TYPE OF REPORT & PERIOD COVERED
Final

6. PERFORMING ORG. REPORT NUMBER

7. AUTHOR(s)
Walter B. Sturek, Donald C. Mylin
Bernard Guidos, and Charles J. Nietubicz

8. CONTRACT OR GRANT NUMBER(s)

9. PERFORMING ORGANIZATION NAME AND ADDRESS
U.S. Army Ballistic Research Laboratory
ATTN: DRDAR-BLL
Aberdeen Proving Ground, Maryland 21005

10. PROGRAM ELEMENT, PROJECT, TASK AREA & WORK UNIT NUMBERS
RDT&E 1L161102AH43

11. CONTROLLING OFFICE NAME AND ADDRESS
US Army Armament Research & Development Command
US Army Ballistic Research Laboratory (DRDAR-BLA-S)
Aberdeen Proving Ground, MD 21005

12. REPORT DATE
June 1983

13. NUMBER OF PAGES
44

14. MONITORING AGENCY NAME & ADDRESS (if different from Controlling Office)

15. SECURITY CLASS. (of this report)
Unclassified

15a. DECLASSIFICATION/DOWNGRADING SCHEDULE

16. DISTRIBUTION STATEMENT (of this Report)
Approved for public release, distribution unlimited.

17. DISTRIBUTION STATEMENT (of the abstract entered in Block 20, if different from Report)

18. SUPPLEMENTARY NOTES

19. KEY WORDS (Continue on reverse side if necessary and identify by block number)
Navier Stokes equations
Projet aerodynamic

20. ABSTRACT (Continue on reverse side if necessary and identify by block number)

Recent papers have reported the application of the thin-layer Parabolized Navier-Stokes (PNS) computational technique to predict the flow over spinning shell at supersonic speeds. This paper reports the results of a computational study using thin layer Navier-Stokes codes to examine the effects of shell nose tip and afterbody geometry. The geometries considered include sharp, hemisphere cap, and flattened nose configurations and a parametric variation of the boattail shape. The results are presented primarily as the aerodynamic coefficients versus Mach number for $1.5 < M < 5$. The Magnus effect is shown to

DD FORM 1 JAN 73 1473 EDITION OF 1 NOV 65 IS OBSOLETE

UNCLASSIFIED

SECURITY CLASSIFICATION OF THIS PAGE (When Data Entered)

20. ABSTRACT (Continued)

be strongly influenced by nose bluntness as well as the geometry of the shell afterbody.

TABLE OF CONTENTS

		Page
	LIST OF ILLUSTRATIONS	5
I.	INTRODUCTION	7
II.	COMPUTATIONAL TECHNIQUE	7
	A. Space Marching Solution	7
	B. Blunt Nose Solution	9
III.	RESULTS	10
	A. Comparisons to Aerodynamic Force Measurements	10
	B. Effect of Boattail Geometry	11
	1. Scope of Computational Effort	11
	2. Aerodynamic Forces versus Axial Position	12
	3. Aerodynamic Coefficients versus Mach Number	12
	C. Effects of Nose Bluntness	13
IV.	SUMMARY	15
	REFERENCES	39
	LIST OF SYMBOLS	41
	DISTRIBUTION LIST	43

LIST OF ILLUSTRATIONS

Figure		Page
1	Coordinates and Notation	16
2	Illustration of Blunt Nose Modeling Geometries	17
3	Model Configuration for Wind Tunnel Test	18
4	Sign Convention for Aerodynamic Forces	19
5	Normal Force Coefficient versus Angle of Attack, Computation Compared to Wind Tunnel Force Measurements, M = 2, Re = 2.49×10^7/m	20
6	Normal Force Coefficient versus Angle of Attack, Computation Compared to Wind Tunnel Force Measurements, M = 3, Re = 2.11×10^7/m	20
7	Magnus Force Coefficient versus Angle of Attack, Computation Compared to Wind Tunnel Force Measurements, M = 2, Re = 2.49×10^7/m, PD/V = .23, $T_w = T_{aw}$	21
8	Magnus Force Coefficient versus Angle of Attack, Computation Compared to Wind Tunnel Force Measurements, M = 3, Re = 2.11×10^7/m, PD/V = .19, $T_w = T_{aw}$	21
9	Model Configurations for Parametric Study	22
10	Normal Force Coefficient versus Axial Position, Parametric Comparison, M = 3, $\alpha = 2°$, $T_w = T_{aw}$	23
11	Magnus Force Coefficient versus Axial Position, Parametric Comparison, M = 3, $\alpha = 2°$, PD/V = .19, $T_w = T_{aw}$, Re = 6.80×10^7/m	24
12	Magnus Force Coefficient versus Axial Position, Parametric Comparison, M = 3, $\alpha = 2°$, PD/V = .19, $T_w = T_{aw}$, Re = 6.80×10^7/m	24
13	Slope of Pitching Moment Coefficient versus Mach No., Parametric Comparison, T_∞ = 294K, T_w = 249K, CG = 3.6 calibers	25
14	Slope of Magnus Moment Coefficient versus Mach No., Parametric Comparison, T_∞ = 294K, T_w = 294K, CG = 3.6 calibers	25
15	Aerodynamics Range Spark Shadowgraph of Artillery Shell at Supersonic Velocity, M ≈ 2.3	26
16	Schlieren Photographs of Wind Tunnel Flow over SOCBT Shell with Sharp, Hemisphere, and Flattened Nose Geometries, M = 3, Re = 9.19×10^6/m	27

LIST OF ILLUSTRATIONS (Cont'd)

Figure		Page
17	Lee Side U-Velocity Profiles at Starting Plane, M = 3, α = 2°, PD/V = 0.19, Atmospheric Flight Conditions, Re = 6.80 × 10^7/m	28
18	Mach Contours of Nose Region Flow for Hemisphere and Flattened Nose Geometries, M = 3, α = 2°, PD/V = 0.19, Atmospheric Flight Conditions, Re = 6.80 × 10^7/m	29
19	Surface Pressure on Hemisphere Nose, M = 3, α = 2°, PD/V = 0.19, Atmospheric Flight Conditions, Re = 6.80 × 10^7/m	30
20	Surface Pressure on Flat Nose, M = 3, α = 2°, PD/V = 0.19, Atmospheric Flight Conditions, Re = 6.80 × 10^7/m	31
21	Lee Side U-Velocity Profiles at X/D = 4.88, SOCBT Model, M = 3, α = 2°, PD/V = 0.19, Atmospheric Flight Conditions, Re = 6.80 × 10^7/m	32
22	Magnus Force versus Axial Position, SOCBT Model Computation Compared to Experimental Force Measurements, M = 3, α = 2°, PD/V = 0.19, Wind Tunnel Test Conditions, Re = 9.19 × 10^6/m	33
23	Magnus Force versus Axial Position, SOCBT Model, M = 3, α = 2°, PD/V = 0.19, Atmospheric Flight Conditions, Re = 6.80 × 10^7/m	34
24	Magnus Force versus Mach Number, SOCBT Model, Comparison between Sharp and Hemisphere Noses, α = 2°, PD/V = 0.19, Atmospheric Flight Conditions	35
25	Slope of Magnus Moment Coefficient versus Mach Number, SOCBT Model, Comparison between Sharp and Hemisphere Noses, Atmospheric Flight Conditions	36
26	Magnus Force Center of Pressure versus Mach Number, SOCBT Model, Comparison between Sharp and Hemisphere Noses, Atmospheric Flight Conditions	37
27	Slope of Pitching Moment Coefficient versus Mach Number, SOCBT Model, Comparison between Sharp and Hemisphere Noses, Atmospheric Flight Conditions	38

I. INTRODUCTION

Recent papers[1,2,3] have reported the development and application of the thin-layer Parabolized Navier-Stokes computational technique to predict the flow about slender bodies of revolution at supersonic velocities. Reference 3 showed the technique to be a viable computational tool for predicting Magnus effects for a six-caliber slender shell with a one-caliber, 7° boattail as verified by comparison to wind tunnel force measurements. The results of Reference 3 represent the first successful efforts to compute the Magnus effect for boattailed shell using sophisticated numerical computational techniques. In this paper, the ability of the PNS computational technique to predict normal and Magnus forces at angles of attack up to 10 degrees and the effects of nose and afterbody geometry on the aerodynamics of shell are examined. The influence of nose bluntness is determined using a starting solution generated by the unsteady Navier-Stokes (time marching) computational technique and then using the PNS (space marching) code to compute the flow over the remainder of the shell.

II. COMPUTATIONAL TECHNIQUE

A. Space Marching Solution

The steady thin-layer Parabolized Navier-Stokes equations can be written for general spatial coordinates ξ, η, ζ as[1]

$$\frac{\partial \hat{E}_s}{\partial \xi} + \frac{\partial \hat{F}}{\partial \eta} + \frac{\partial \hat{G}}{\partial \zeta} = \frac{1}{\hat{Re}} \frac{\partial \hat{S}}{\partial \zeta} \tag{1}$$

where

$\xi = \xi(x)$ is the streamwise (marching) coordinate

$\eta = \eta(x,y,z)$ is the circumferential coordinate

$\zeta = \zeta(x,y,z)$ is the normal coordinate

---

1. *Schiff, L.B., and Steger, J.L., "Numerical Simulation of Steady Supersonic Viscous Flow," AIAA Journal, Vol. 18, No. 12, December 1980, pp. 1421-1430.*

2. *Schiff, L.B., and Sturek, W.B., "Numerical Simulation of Steady Supersonic Flow Over an Ogive-Cylinder-Boattail Body," AIAA Paper No. 80-0066, AIAA 18th Aerospace Sciences Meeting, January 1980.*

3. *Sturek, W.B., and Schiff, L.B., "Computations of the Magnus Effect for Slender Bodies in Supersonic Flow," AIAA Paper No. 80-1586-CP, AIAA Atmospheric Flight Mechanics Conference, August 1980.*

The inviscid flux vectors in Eq. (1) are

$$\hat{E}_s = J^{-1}\begin{bmatrix} \rho U \\ \rho uU+\xi_x p_s \\ \rho vU \\ \rho wU \\ (e+p_s)U \end{bmatrix}, \quad \hat{F} = J^{-1}\begin{bmatrix} \rho V \\ \rho uV+\eta_x p \\ \rho vV+\eta_y p \\ \rho wV+\eta_z p \\ (e+p)V \end{bmatrix}, \quad \hat{G} = J^{-1}\begin{bmatrix} \rho W \\ \rho uW+\zeta_x p \\ \rho vW+\zeta_y p \\ \rho wW+\zeta_z p \\ (e+p)W \end{bmatrix}$$

The vector $\hat{q}(\rho, \rho u, \rho v, \rho w, e)$ contains the dependent variables. Variations of body geometry are included in Eq. (1) through the presence of the metric terms η_x, η_y, η_z, etc., which appear in the flux vectors and through the Jacobian J, of the transformation from the physical space to the computational space. The thin-layer viscous term, valid for high Reynolds No. flow, is

$$\hat{S} = J^{-1}\begin{bmatrix} 0 \\ \mu(\zeta_x^2+\zeta_y^2+\zeta_z^2)u_\zeta + (\mu/3)(\zeta_x u_\zeta+\zeta_y v_\zeta+\zeta_z w_\zeta)\zeta_x \\ \mu(\zeta_x^2+\zeta_y^2+\zeta_z^2)v_\zeta + (\mu/3)(\zeta_x u_\zeta+\zeta_y v_\zeta+\zeta_z w_\zeta)\zeta_y \\ \mu(\zeta_x^2+\zeta_y^2+\zeta_z^2)w_\zeta + (\mu/3)(\zeta_x u_\zeta+\zeta_y v_\zeta+\zeta_z w_\zeta)\zeta_z \\ \{(\zeta_x^2+\zeta_y^2+\zeta_z^2)\,[(\mu/2)(u^2+v^2+w^2)_\zeta + \kappa Pr^{-1}(\gamma-1)^{-1}(a^2)_\zeta] \\ \quad + (\mu/3)\,(\zeta_x u + \zeta_y v + \zeta_z w)(\zeta_x u_\zeta + \zeta_y v_\zeta + \zeta_z w_\zeta)\} \end{bmatrix}$$

Equation 1 is parabolic-like with respect to ξ and can thus be marched downstream in the ξ direction from an initial data plane (subject to appropriate body and free stream boundary conditions) under those conditions where the local flow is supersonic.

The numerical algorithm used to march Eq. (1) downstream is an approximately factored, fully implicit, finite-difference scheme. The algorithm is conservative and of second-order accuracy in the marching direction. A two-layer, algebraic eddy viscosity model[4] is included for the computation of turbulent flows. Details of the Parabolized Navier-Stokes assumption and the derivation of the algorithm are included in Reference 1.

---

4. *Baldwin, B.S., and Lomax, H., "Thin Layer Approximation and Algebraic Model for Separated Turbulent Flows," AIAA Paper No. 78-257, 1978.*

The computations are started from a converged conical solution near the tip of the projectile. The full solution is then obtained by marching over the body in the streamwise (axial) direction. This marching technique is depicted in Figure 1 along with the coordinate system. A logarithmic stretching is used to achieve adequate grid resolution of the turbulent viscous layer. The grid generator employs an adaptive capability which insures that adequate resolution of the viscous layer is maintained over the full length of the model. The streamwise marching stepsize was adjusted to yield 500 to 800 computational steps for the full length of the shell. The computational grid consisted of 36 stations about the circumference of the model ($\Delta\phi = 10°$) and 50 points between the body and the outer boundary.

B. Blunt Nose Solution

The solution for the flow over the blunt nose of the shell has been obtained using the three dimensional thin-layer Navier-Stokes solver recently reported by Chaussee, Kutler and Pulliam.[5] This is a fully implicit computational technique which solves for the entire flow field by converging to a steady flow solution. The outer boundary for this code employes a shock-fitting scheme. Since the solution is obtained for only a small flow field region near the nose, good grid resolution has been achieved. The grid used consisted of 30 points from the body to the outer boundary, 20 points axially along the surface of the shell, and 36 points circumferentially around the shell.

The nose region has initially been modeled as a hemisphere cone. The conical extension is of sufficient length to achieve a well established supersonic conical flow in order to apply the zero gradient outflow boundary condition with confidence. This modeling of the nose region is depicted schematically in Figure 2. The bluntness ratio is defined to be the ratio of the diameter of the cone at the forward tangency point to the maximum diameter of the shell.

In addition to the hemisphere blunt nose, several cases have been run for a flattened nose. The intent is to model as closely as possible the meplate (flat face) configuration of typical Army fuze.

The time-dependent thin-layer Navier-Stokes equations can be written in strong conservation-law form as

$$\frac{\partial \hat{q}}{\partial \tau} + \frac{\partial \hat{E}}{\partial \xi} + \frac{\partial \hat{F}}{\partial \eta} + \frac{\partial \hat{G}}{\partial \zeta} = \frac{1}{\hat{Re}} \frac{\partial \hat{S}}{\partial \zeta} \tag{2}$$

---

5. *Chaussee, D.S., Kutler, P., and Pulliam, T.H., "Three Dimensional Viscous Flow Field Program; Part I: Viscous Blunt Body Program (Interim Report)," AFWL-TM-81-63-FIMG, March 1981.*

where $\tau = t$ is the time (marching)

$\xi = \xi(t, x, y, z)$ is the longitudinal coordinate

$\eta = \eta(t, x, y, z)$ is the circumferential coordinate

$\zeta = \zeta(t, x, y, z)$ is the near normal coordinate

The inviscid flux vectors are $\hat{E}$, $\hat{F}$, $\hat{G}$ and contain terms for the conservation of mass, momentum, and energy in the three coordinate directions. The vector $\hat{q}(\rho, \rho u, \rho v, \rho w, e)$ contains the dependent variables. The $\hat{S}$ matrix contains the viscous terms which are valid for high Reynolds number flows.

The contravarient velocity components are

$$U = \xi_x u + \xi_y v + \xi_z w$$

$$V = \eta_x u + \eta_y v + \eta_z w$$

$$W = \zeta_x u + \zeta_y v + \zeta_z w.$$

Variations of body geometry are included in Equation (2) through the presence of metric terms (ξ_x, η_x, etc.) and the Jacobian J, which appear in the flux vectors and contravariant velocities. A two-layer algebraic eddy viscosity model is used for the turbulent viscous solutions.

III. RESULTS

A. Comparisons to Aerodynamic Force Measurements

In Reference 3 a series of results obtained for $\alpha = 2°$ were compared to experimental measurements (Reference 6) of aerodynamic forces for $2 < M < 4$. The model configuration for this study is shown in Figure 3. The sign convention for the aerodynamic forces is shown in Figure 4. The results in Reference 3 indicated that the thin-layer PNS computational technique achieved excellent agreement in comparison to experimental measurements of aerodynamic forces including the Magnus effect. Comparisons of the PNS computed results to experiment have now been carried out for $\alpha < 10°$. Computed results were obtained for $\alpha = 2°$, 4°, 6°, and 10°.

---

6. *Nietubicz, C.J., and Opalka, K., "Supersonic Wind Tunnel Measurements of Static and Magnus Aerodynamic Coefficients for Projectile Shapes with Tangent and Secant Ogive Noses," ARBRL-MR-02991, U.S. Army Ballistic Research Laboratory/ARRADCOM, Aberdeen Proving Ground, MD 21005, February 1980 (AD A083297).*

Comparisons between computation and experiment are shown as a function of angle of attack for normal force for M = 2 and M = 3 in Figures 5 and 6, respectively. Results for two boattail configurations are shown. The notation SOCBT depicts the 7°, one caliber boattail model in Figure 3. The notation SOC depicts a model with a 0° boattail. Excellent agreement is achieved for $\alpha \leq 10°$ for magnitude as well as the nonlinear behavior of the normal force coefficient.

A similar comparison is shown for Magnus force for M = 2 and M = 3 in Figures 7 and 8, respectively. These results indicate very good agreement between computation and experiment for $\alpha \leq 6°$. However, the computed results for $\alpha = 10°$ are not in close agreement with the trend of the experimental data for $\alpha > 6°$. This is more clearly indicated in Figure 8. This discrepancy is not unexpected since, as shown in Reference 2 where comparisons between computation and experiment for surface pressure were made, good agreement was achieved at $\alpha = 6.3°$ and significantly less satisfactory agreement was obtained at $\alpha = 10.4°$. The discrepancy at $\alpha = 10.4°$ was attributed to the inability of the computational technique to accurately model the significant development of lee-side vortical flow.

The ability of the computational technique to accurately predict Magnus for $\alpha \leq 6°$ does represent a significant capability. This demonstrates that useful engineering results can be achieved for highly three-dimensional flow fields using a very simple turbulence model.

B. Effect of Boattail Geometry

1. Scope of Computational Effort.

A series of computations have been accomplished for a parametric variation of boattail configuration. The geometries are shown in Figure 9 and include boattail lengths of one and two calibers for boattail angles of 0°, 5°, 7-1/2°, and 10°. This range of boattail length and angle effectively spans the range for practical shell application.

The computations were accomplished for standard atmospheric and wall temperature conditions commonly encountered in projectile firing tests. These conditions are summarized in Table 1.

TABLE 1. SUMMARY OF BOUNDARY CONDITIONS FOR PARAMETRIC COMPUTATIONS

MACH No.	α, degrees	PD/V	T_∞, °K	p_∞, atm	T_w, °K
2	2	.19	294	1	239,294,325
3	2	.19	294	1	239,294,325
4	2	.19	294	1	239,294,325

MACH No.	FREE STREAM REYNOLDS NO.
2	4.53×10^7/m
3	6.80×10^7/m
4	9.06×10^7/m

2. Aerodynamic Forces versus Axial Position.

The development of the normal force as a function of axial position is shown in Figure 10 for boattail angles of 0° and 7-1/2° comparing results for one and two caliber lengths of the boattail. The normal force increases monotonically for the 0° boattail in contrast to the behavior for the 7-1/2° boattails where the normal force reaches a maximum and then decreases as the boattail length increases.

The development of the Magnus force as a function of axial position is shown in Figures 11 and 12 comparing the effects of boattail length (Figure 11) and boattail angle (Figure 12). Figure 11 shows that the length of the boattail strongly affects the magnitude of the Magnus force. Figure 12 shows that the Magnus force increases monotonically for increasing boattail angle for the cases considered here.

3. Aerodynamic Coefficients versus Mach Number.

Parametric comparisons for pitch and yaw plane aerodynamic parameters are shown in Figures 13 and 14. These examples illustrate the ability of the computational technique to develop data which reflect the effects of body configuration and Mach number.

The effect of boattail angle and length for the slope of the pitching moment (CG = 3.6 calibers) is shown in Figure 13. These results show that both boattail length and angle have a significant effect on the pitching moment. The trends indicate that C_{M_α} is increased for increasing boattail angle and boattail length. This trend is accentuated for flow velocities near Mach = 2.

The slope of the Magnus moment coefficient (CG = 3.6 calibers) is shown in Figure 14. The effect of boattail length is seen to strongly affect the Magnus moment coefficient. The trend illustrated is that $C_{M_{p\alpha}}$ is increased as boattail length and angle are increased.

C. Effects of Nose Bluntness

A spark shadowgraph of an artillery shell at a speed of approximately Mach = 2.25 taken in the BRL Transonic Range is shown in Figure 15. This shadowgraph shows the detached bow shock that occurs for supersonic flow over artillery shell. Note the presence of a shock at the sharp corner of the flattened nose. This shock is caused by the local flow separation which is induced by the strong expansion at the sharp corner.

A recent wind tunnel test[7] was performed in which aerodynamic force measurements were made for spinning models with sharp, hemisphere, and flattened nose tips. A Schlieren photograph of the flow over these nose tips at Mach = 3 is shown in Figure 16. It is obvious that the bow shock pattern is different for each of these configurations. The inner shock at the nose tip that is very distinct in Figure 15 also occurs at the sharp corner of the flattened nose in Figure 16. This shock is not visible for the hemisphere nose. The shock waves starting about one diameter downstream of the model nose are generated by a boundary layer trip.

In this portion of the study, the significance of the technique for modeling the nose region of spinning shell on the predicted aerodynamic behavior at supersonic velocities is examined. The model geometry used is the ogive-cylinder-boattail (SOCBT) shape shown in Figure 3. Figure 2 shows the nose tip geometries in detail. Flow field computations have been obtained for wind tunnel test conditions and for free flight atmospheric conditions. The wall temperature boundary condition has been modeled as an adiabatic wall for the wind tunnel tests and as a constant wall temperature equal to the atmospheric temperature for the atmospheric flight conditions.

Examples of u-velocity profiles at the starting plane for sharp and blunt noses are shown in Figure 17. The profile for the blunt nose cases are significantly distorted in the inviscid flow region compared to the sharp nose case which has a comparatively flat profile. An interesting comparison is shown in Figure 18 which illustrates Mach contours for the blunt starting solutions. The more severe flow expansion around the flattened nose compared to the hemisphere nose is clearly illustrated. Figures 19 and 20 show the distribution of surface pressure for windward and leeward rays for the two blunt nose shapes.

Additional examples of u-velocity profiles for the different nose configurations are shown in Figure 21 for a longitudinal station near the start of the boattail. Small but distinct differences are apparent upon comparison of

---

7. *Unpublished Wind Tunnel Data. Test performed at the Naval Surface Weapons Center, White Oak Laboratory, Silver Spring, Maryland, for the U.S. Army Ballistic Research Laboratory.*

these profiles indicating that the effect of the initial conditions does not wash out rapidly.

The wind tunnel test[7] conducted recently for the BRL at the Naval Surface Weapons Center, White Oak Laboratory obtained measurements of the aerodynamic forces on the slender shell with sharp, hemisphere, and flattened nose configurations. Force balance measurements were obtained for pitch plane and Magnus forces. Computational results for sharp and hemisphere nose geometries have been obtained for comparison to these data. The computational and experimental results for Magnus force are compared in Figure 22. The experimental data indicate an increasing Magnus force for increasing nose flatness. The agreement between computation and experiment for the sharp and hemisphere nose configurations is quite good. However, there is substantial disagreement between computation and experiment for the flattened nose geometry. The computation for the hemisphere and the flattened nose yielded virtually identical results. This is in sharp contrast to the experimental results which yielded a substantially greater Magnus force for the flat nose case than that for the hemisphere cap. Further computations for which the boundary layer on the nose cap was laminar yielded results that were virtually identical to the results for which the boundary layer on the nose cap was turbulent. A possible cause for the discrepancy is the difference between the flatness of the nose for the computational model and the model used in the wind tunnel test. As shown in Figure 2, the flat part of the nose does not extend to the full diameter of the meplate. Additional computations are planned in which the actual flatness of the fuze configuration will be modeled more closely. It would also be useful to have experimental data for a wider range of free stream Mach number for comparison to the computations.

An example is shown in Figure 23 of the development of the Magnus force as a function of axial position comparing computational results for sharp, hemisphere, and flattened nose configurations for atmospheric flight conditions. The results indicate a significant increase in the Magnus force for the blunt noses. The trend of increasing Magnus force for increasing nose flatness is observed. Examples of the Magnus force as a function of Mach number for the sharp and hemisphere blunt noses are shown in Figure 24. The blunt case is consistently greater in absolute magnitude than the sharp case.

The slope of the Magnus moment coefficient as a function of Mach number is shown in Figure 25 comparing results for sharp and hemisphere noses. Again, the blunt nose results are consistently greater than those for the sharp nose. The results also predict a greater influence of nose bluntness as the Mach number decreases. The behavior of the Magnus center of pressure is shown in Figure 26. These results indicate that the Magnus center of pressure is: (1) located well downstream of the CG location (3.6 calibers), (2) weakly sensitive to Mach number, and (3) not highly sensitive to the nose bluntness.

The slope of the pitching moment coefficient as a function of Mach number is shown in Figure 27. These results indicate that the pitching moment is not sensitive to small nose bluntness typical of artillery shell.

IV. SUMMARY

A computational study has been described in which thin-layer Navier-Stokes computational techniques have been employed to predict the aerodynamics of slender, spinning shell at supersonic velocities.

Results have been discussed which illustrate the ability of the computational technique to accurately predict Magnus and normal forces for angles of attack up to six degrees. Parametric results showing the effects of boattail length and boattail angle were discussed for pitching moment and Magnus moment.

Comparisons have been shown between results obtained in which the nose tip of the shell has been modeled as a sharp cone, a hemisphere-cone, and a truncated cone. The results indicate that small nose bluntness, typical of artillery shell, can significantly increase the Magnus moment. The results further indicate that the pitching moment is not strongly affected by the small nose bluntness considered in this study.

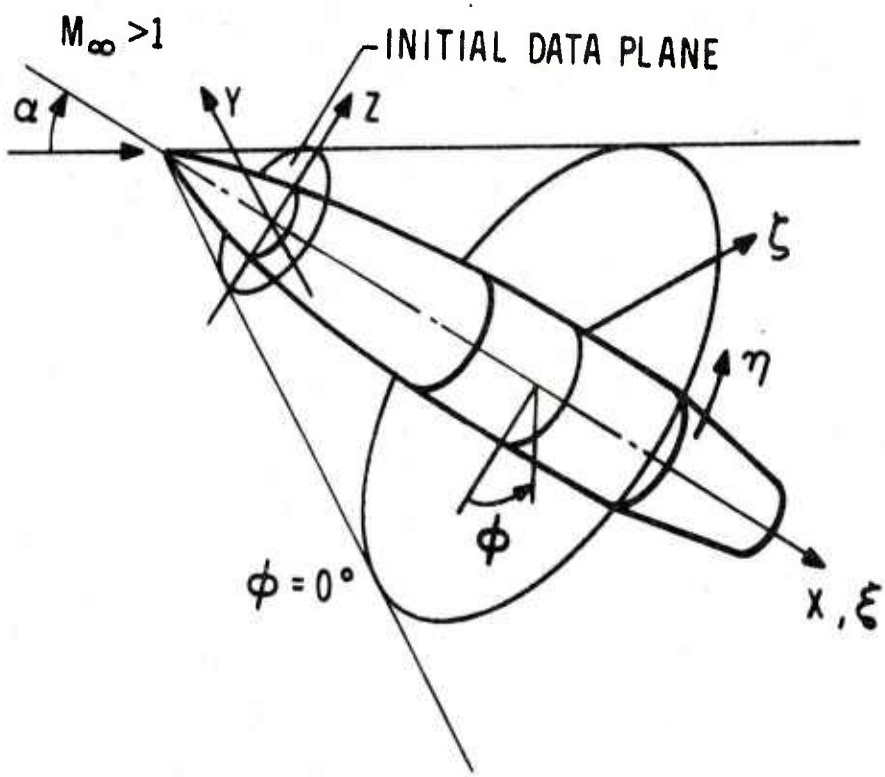

Figure 1. Coordinates and Notation.

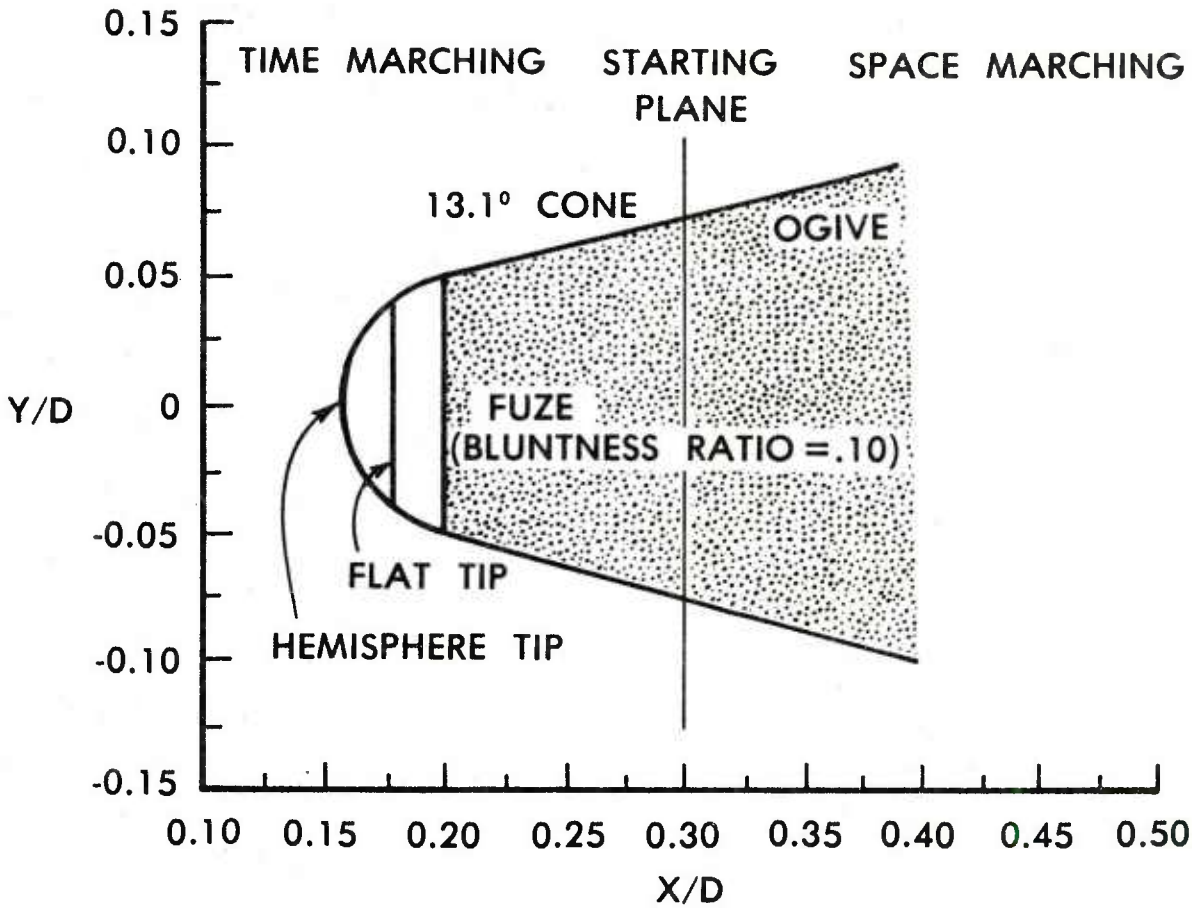

Figure 2. Illustration of Blunt Nose Modeling Geometries.

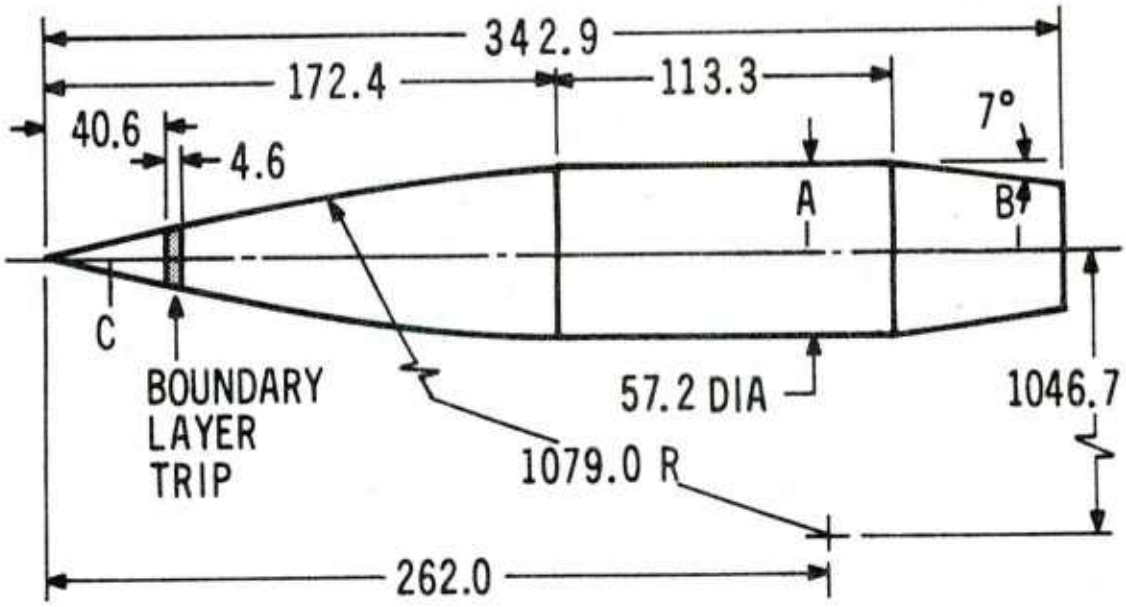

NOTE: DIMENSIONS ARE IN MILLIMETRES
A,B BOUNDARY LAYER SURVEY STATIONS
C CONICAL STARTING SOLUTION STATION

Figure 3. Model Configuration for Wind Tunnel Test.

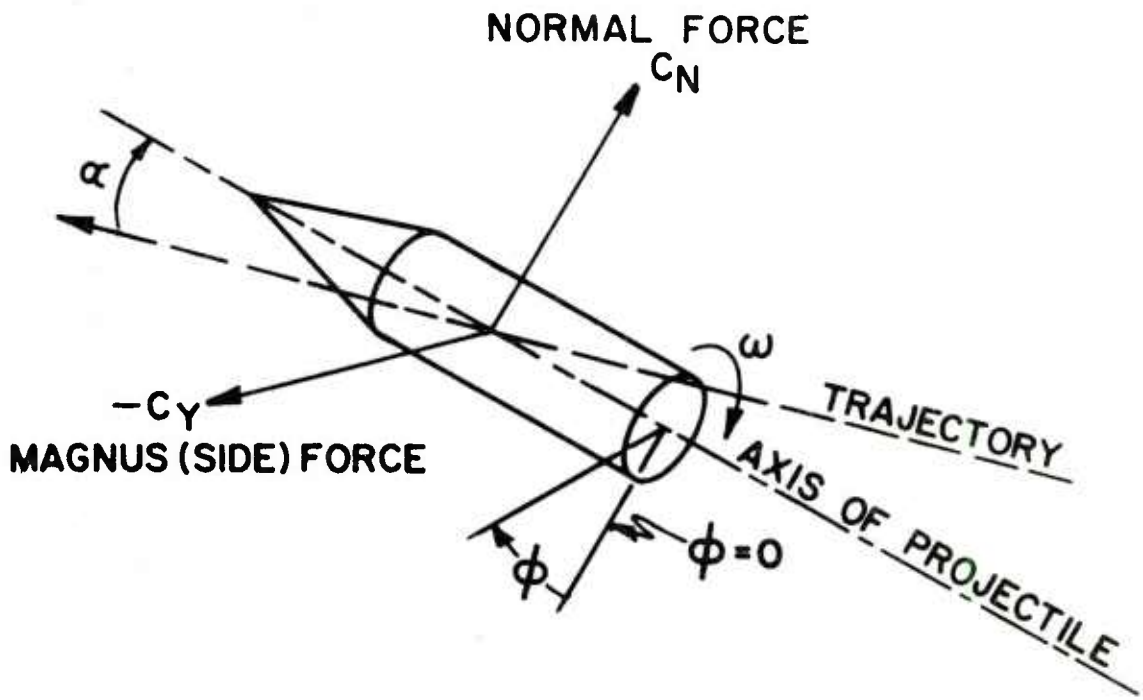

Figure 4. Sign Convention for Aerodynamic Forces.

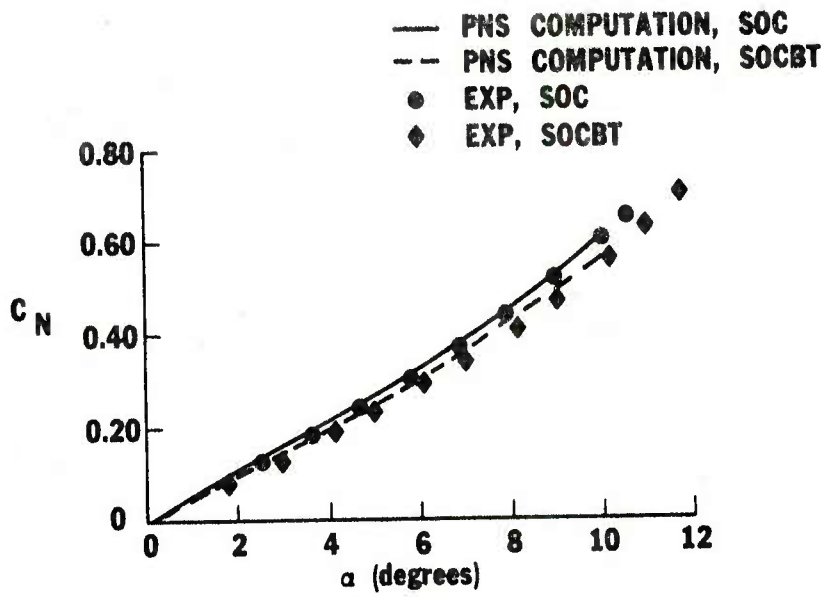

Figure 5. Normal Force Coefficient versus Angle of Attack, Computation Compared to Wind Tunnel Force Measurements, M = 2, Re = 2.49 × 10^7/m

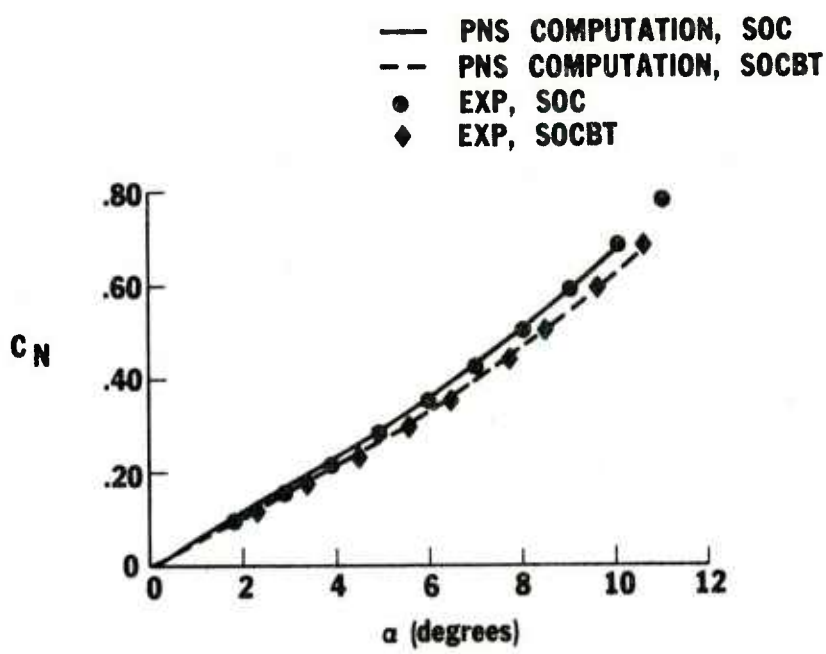

Figure 6. Normal Force Coefficient versus Angle of Attack, Computation Compared to Wind Tunnel Force Measurements, M = 3, Re = 2.11 × 10^7/m

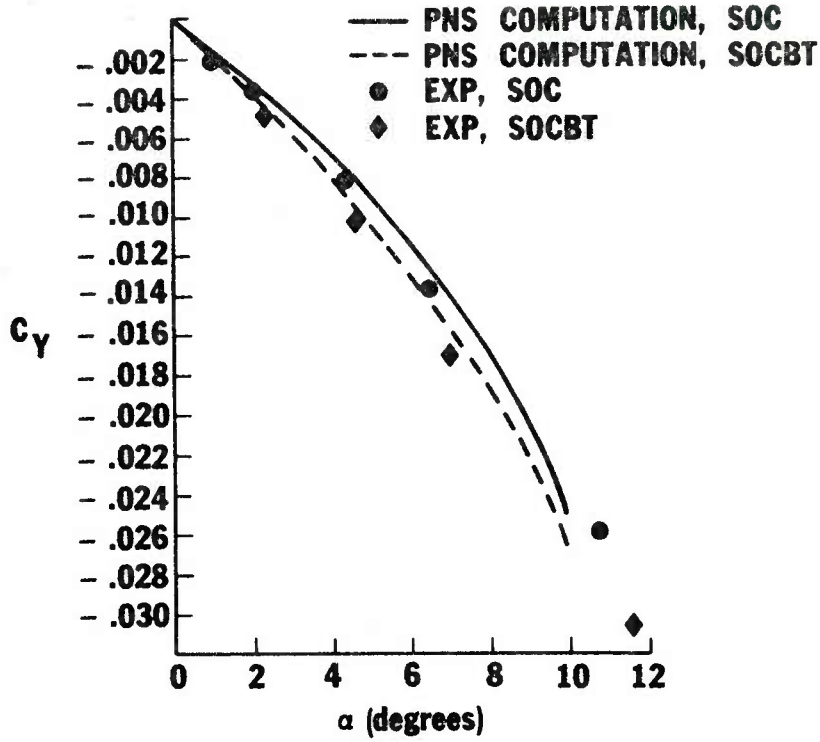

Figure 7. Magnus Force Coefficient versus Angle of Attack, Computation Compared to Wind Tunnel Force Measurements, M = 2, Re = 2.49×10^7/m, PD/V = .23, $T_w = T_{aw}$

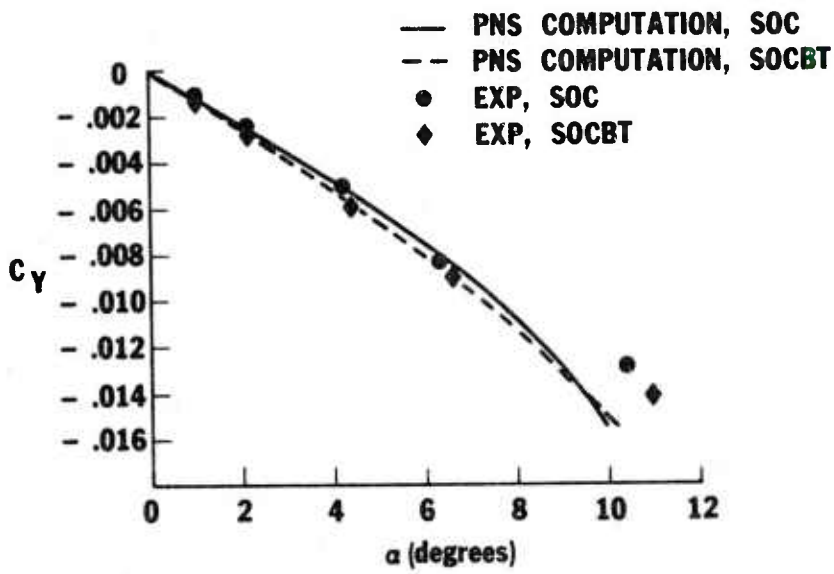

Figure 8. Magnus Force Coefficient versus Angle of Attack, Computation Compared to Wind Tunnel Force Measurements, M = 3, Re = 2.11×10^7/m, PD/V = .19, $T_w = T_{aw}$

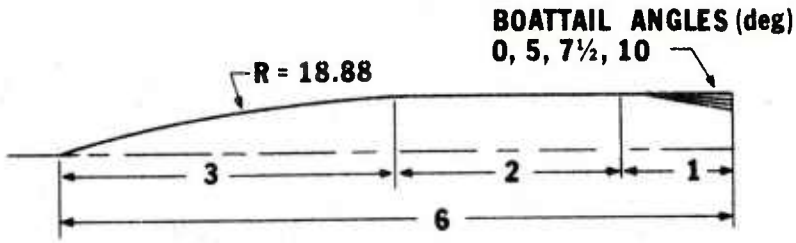

ONE CALIBER BOATTAIL MODEL

NOTE: All dimensions in calibers

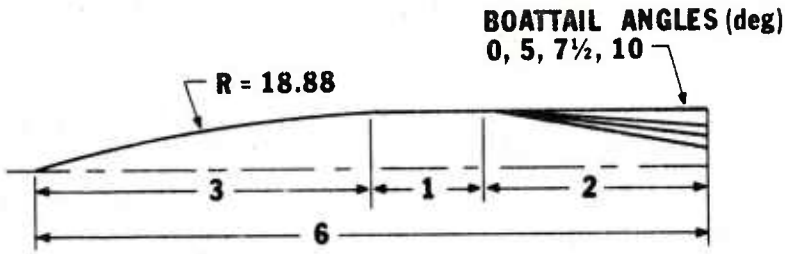

TWO CALIBER BOATTAIL MODEL

Figure 9. Model Configurations for Parametric Study

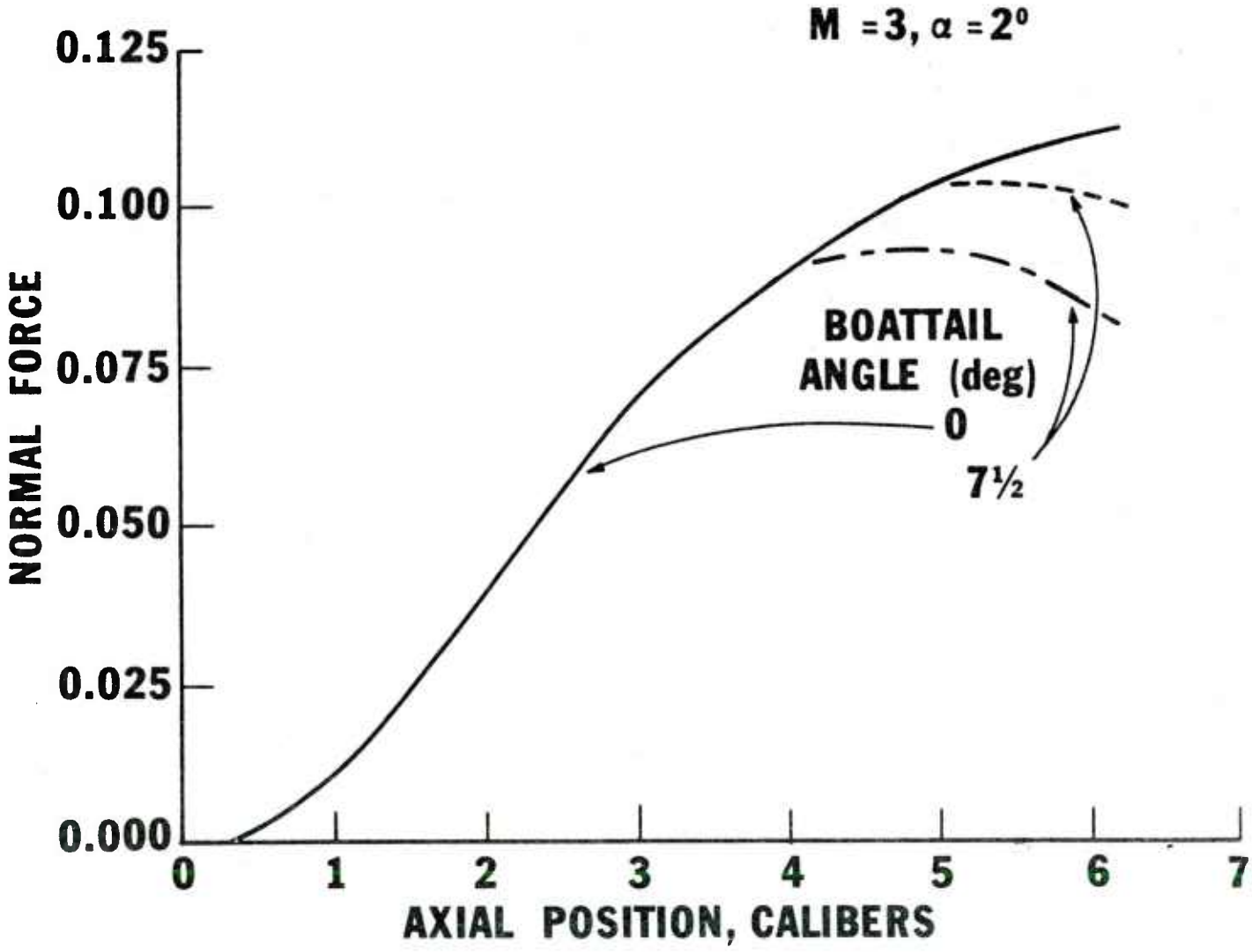

Figure 10. Normal Force Coefficient versus Axial Position, Parametric Comparison, $M = 3$, $\alpha = 2°$, $T_w = T_{aw}$

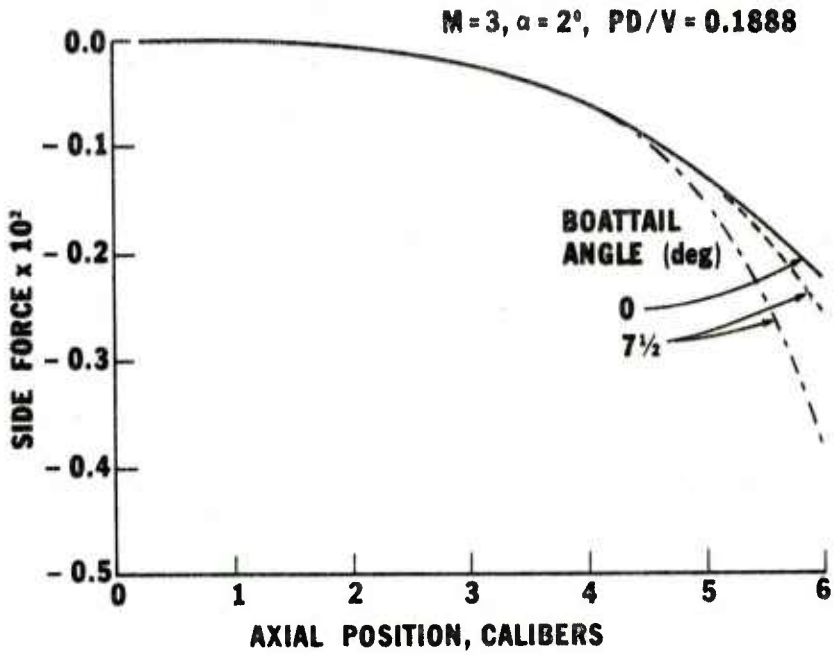

Figure 11. Magnus Force Coefficient versus Axial Position, Parametric Comparison, M = 3, α = 2°, PD/V = .19, $T_w = T_{aw}$, Re = 6.80 × 10^7/m

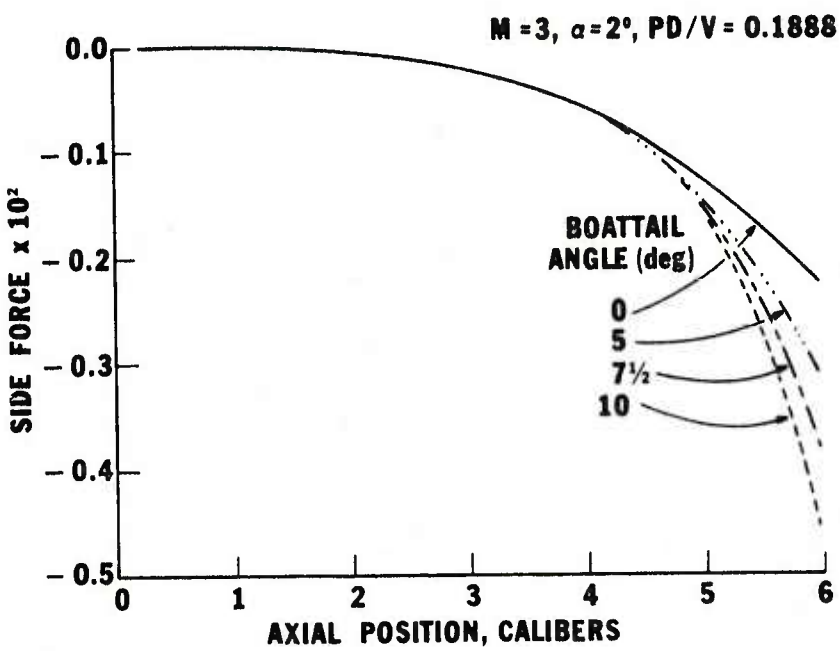

Figure 12. Magnus Force Coefficient versus Axial Position, Parametric Comparison, M = 3, α = 2°, PD/V = .19, $T_w = T_{aw}$, Re = 6.80 × 10^7/m

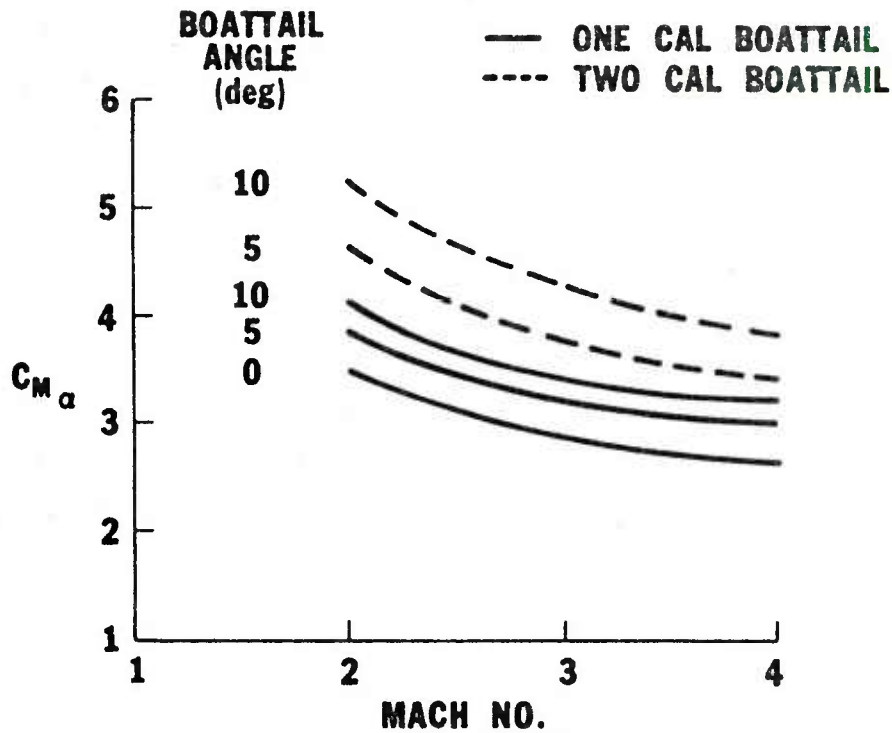

Figure 13. Slope of Pitching Moment Coefficient versus Mach No., Parametric Comparison, T_∞ = 294K, T_W = 294K, CG = 3.6 calibers

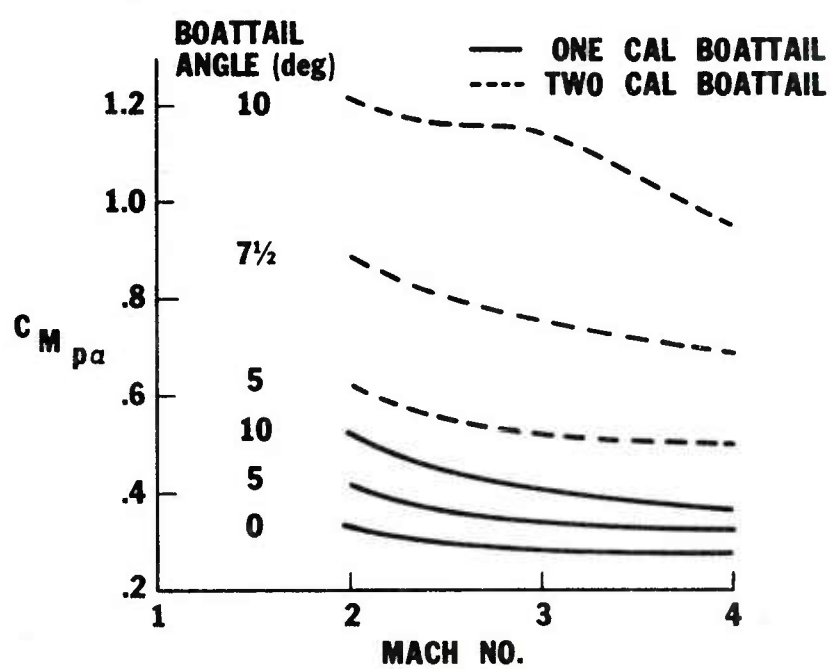

Figure 14. Slope of Magnus Moment Coefficient versus Mach No., Parametric Comparison, T_∞ = 294K, T_W = 294K, CG = 3.6 calibers

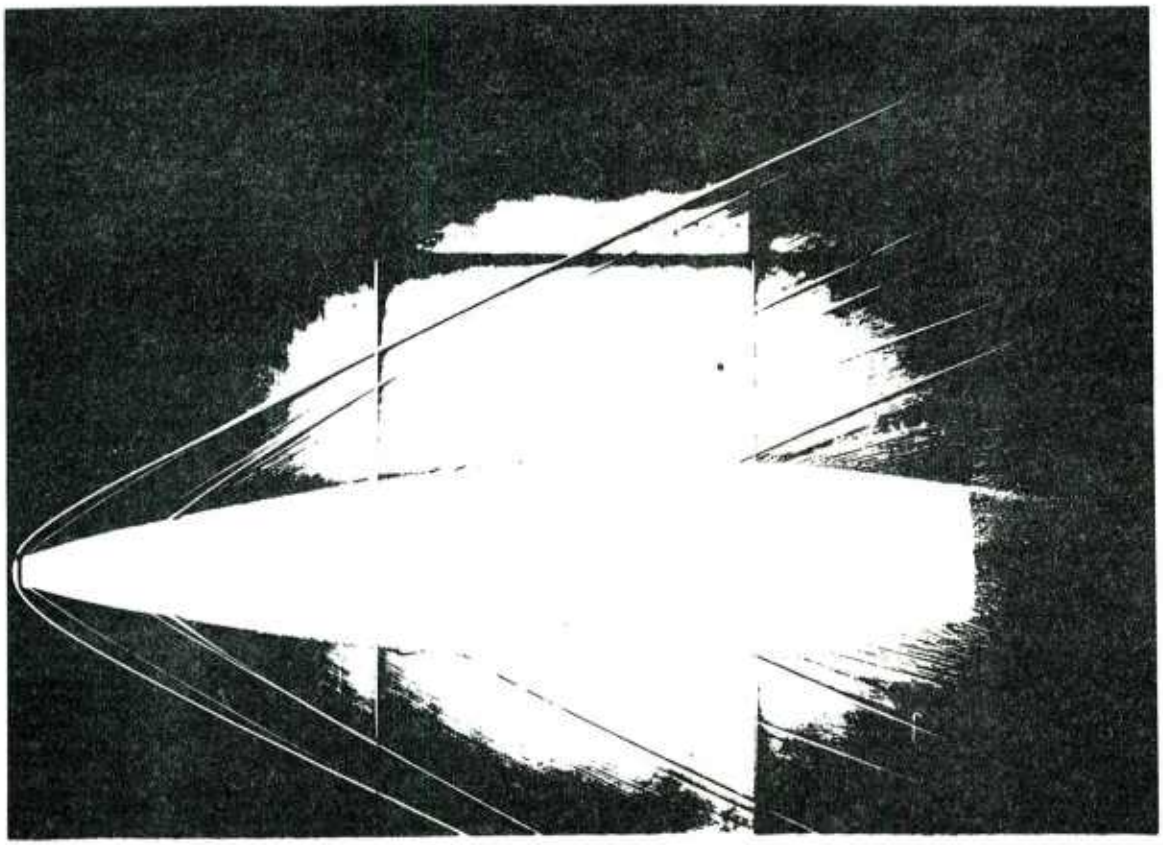

Figure 15. Aerodynamics Range Spark Shadowgraph of Artillery Shell at Supersonic Velocity, M ≈ 2.3

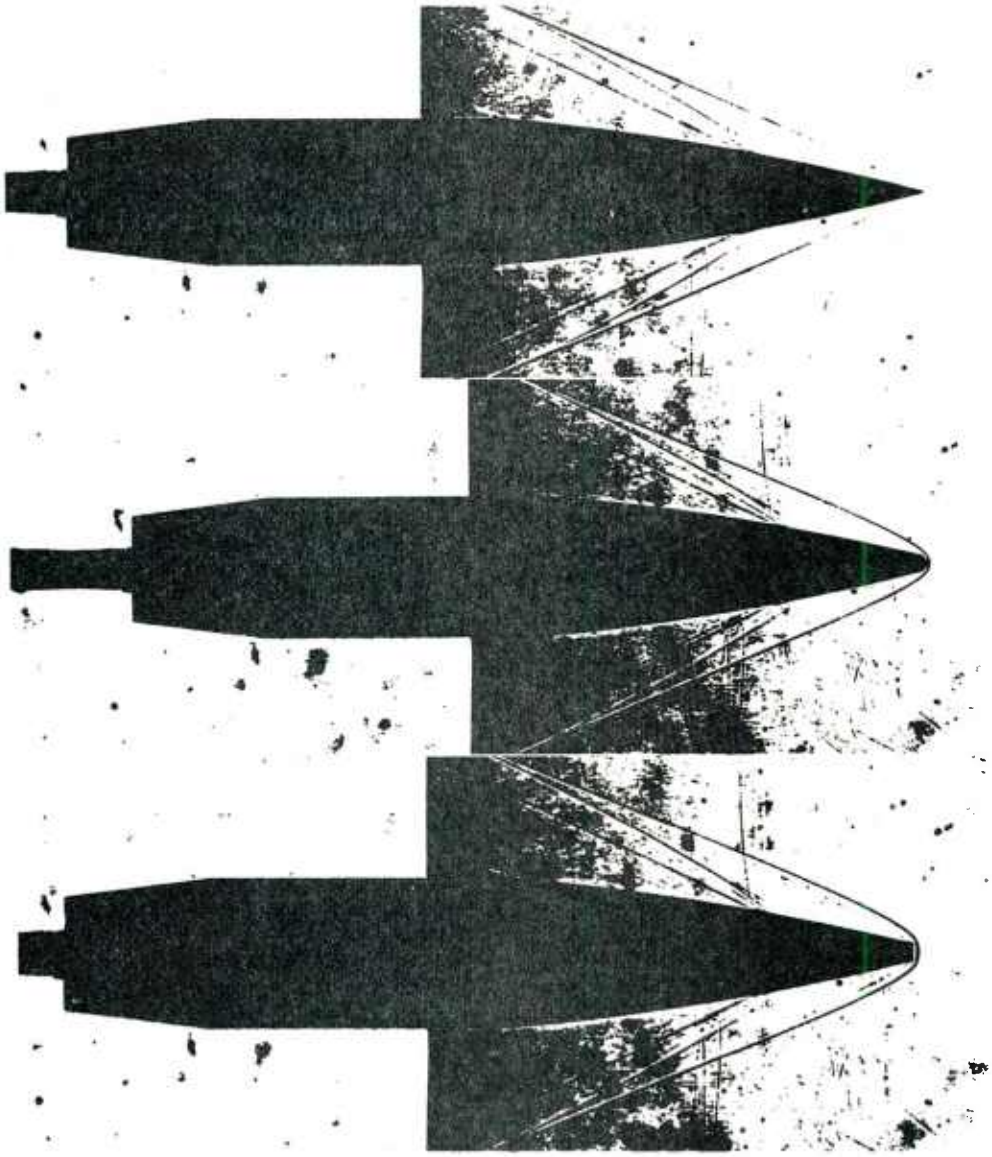

Figure 16. Schlieren Photographs of Wind Tunnel Flow over SOCBT Shell with Sharp, Hemisphere, and Flattened Nose Geometries, M = 3, Re = 9.19×10^6/m

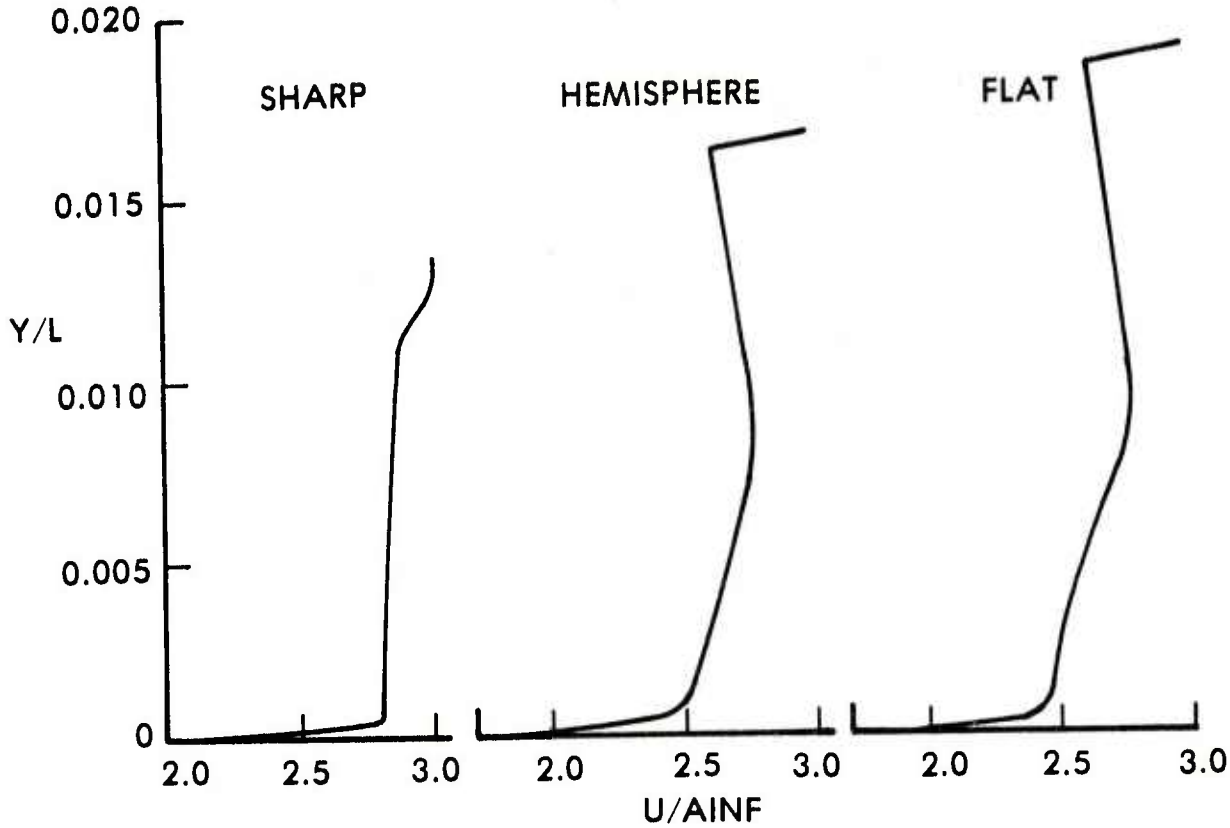

Figure 17. Lee Side U-Velocity Profiles at Starting Plane, M = 3, α = 2°, PD/V = 0.19, Atmospheric Flight Conditions, Re = 6.80×10^7/m

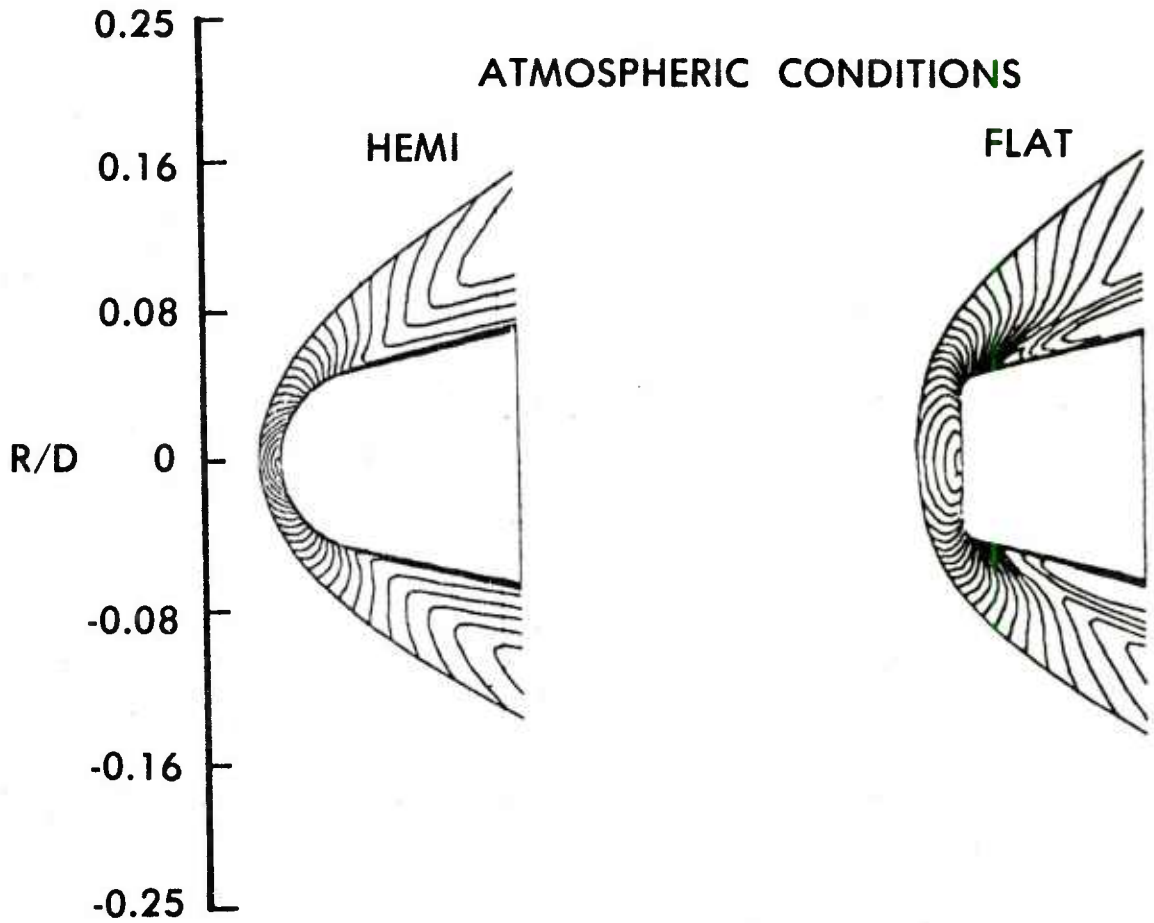

Figure 18. Mach Contours of Nose Region Flow for Hemisphere and Flattened Nose Geometries, M = 3, α = 2°, PD/V = 0.19, Atmospheric Flight Conditions, Re = 6.80×10^7/m

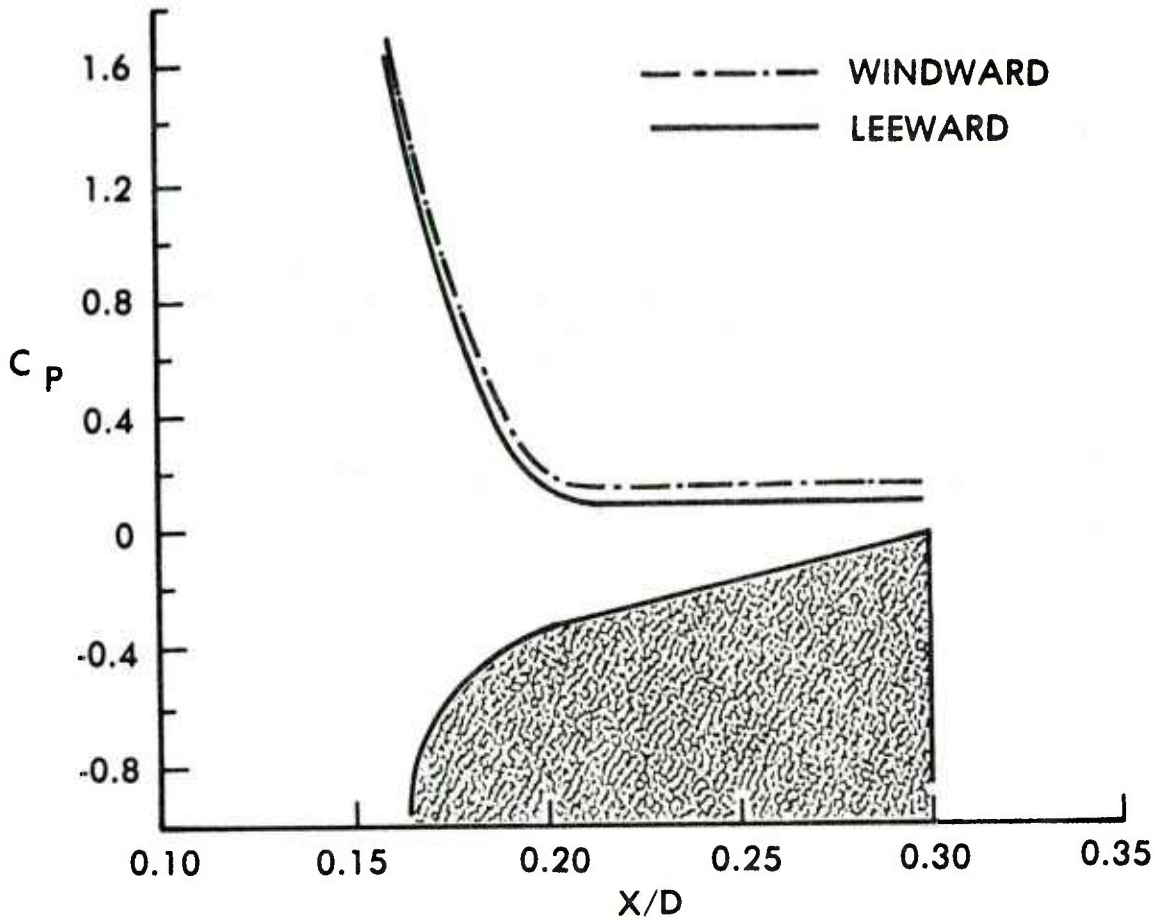

Figure 19. Surface Pressure on Hemisphere Nose, M = 3, α = 2°, PD/V = 0.19, Atmospheric Flight Conditions, Re = 6.80×10^7/m

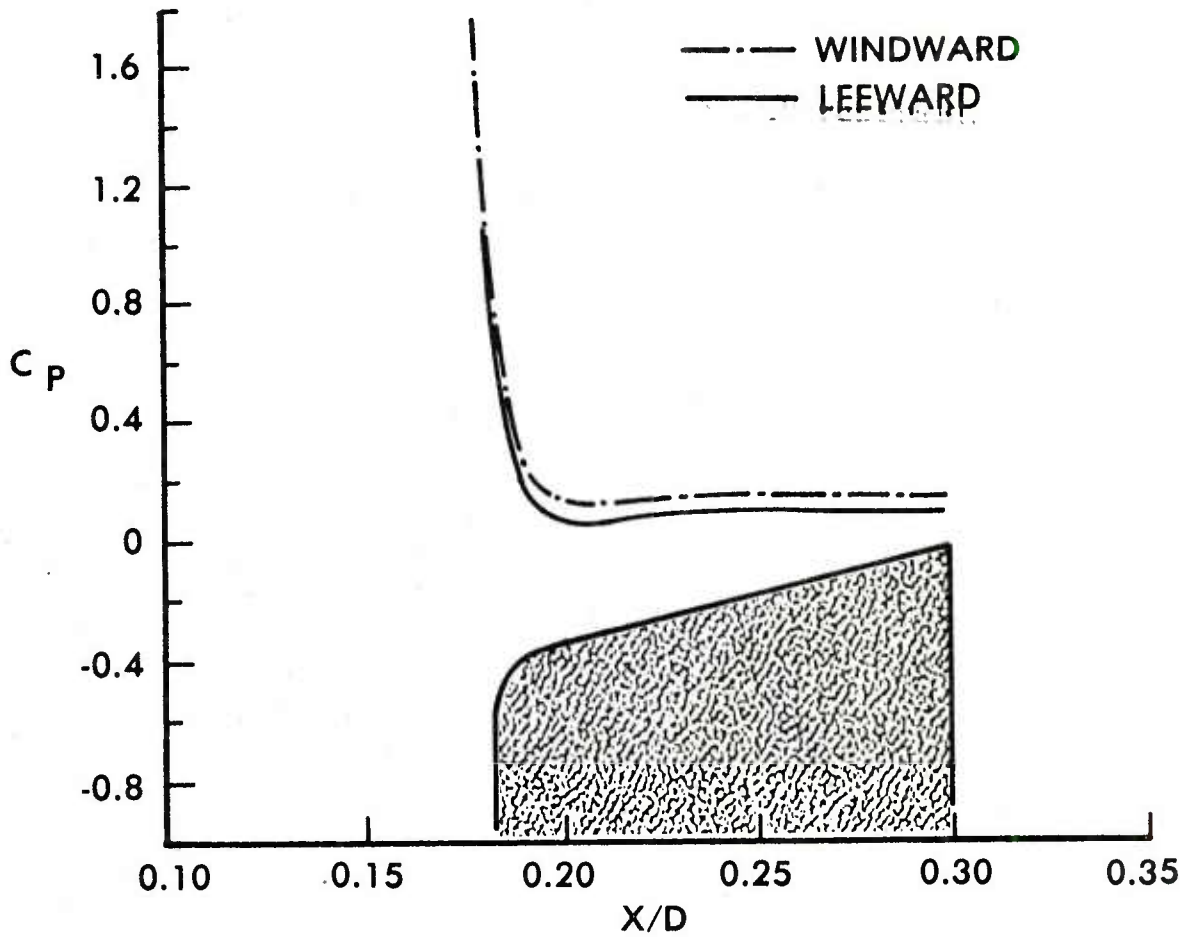

Figure 20. Surface Pressure on Flat Nose, M = 3, α = 2°, PD/V = 0.19, Atmospheric Flight Conditions, Re = 6.80×10^7/m

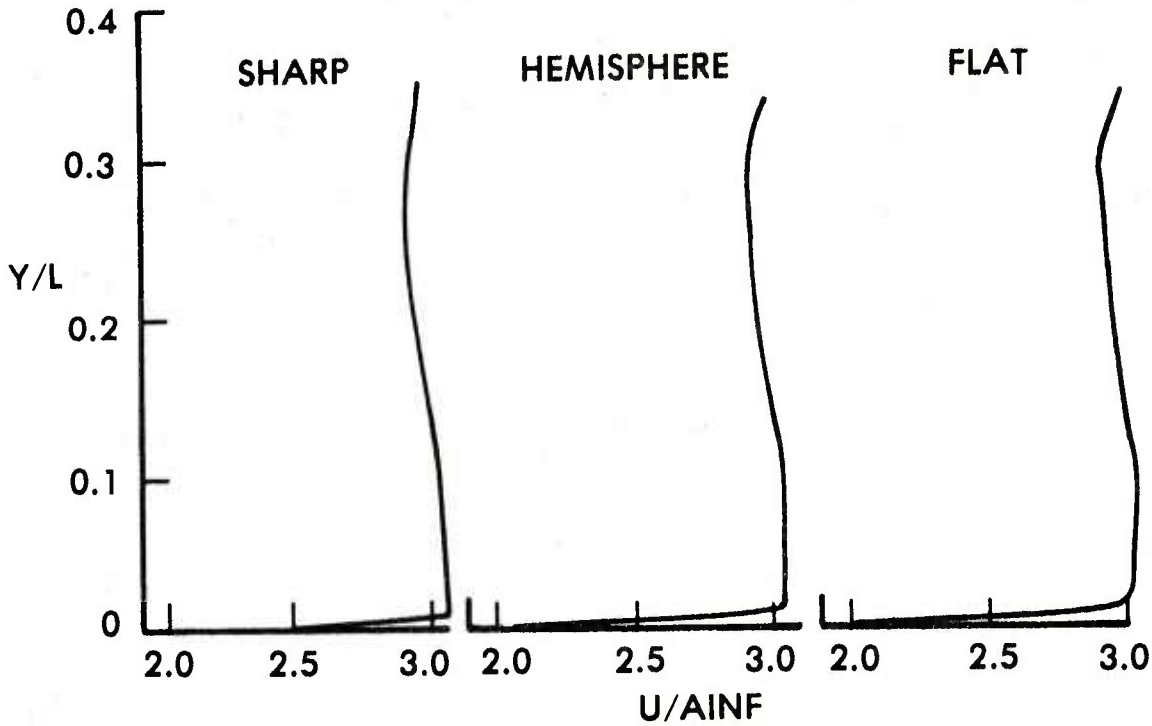

Figure 21. Lee Side U-Velocity Profiles at X/D = 4.88, SOCBT Model, M = 3, α = 2°, PD/V = 0.19, Atmospheric Flight Conditions, Re = 6.80×10^7/m

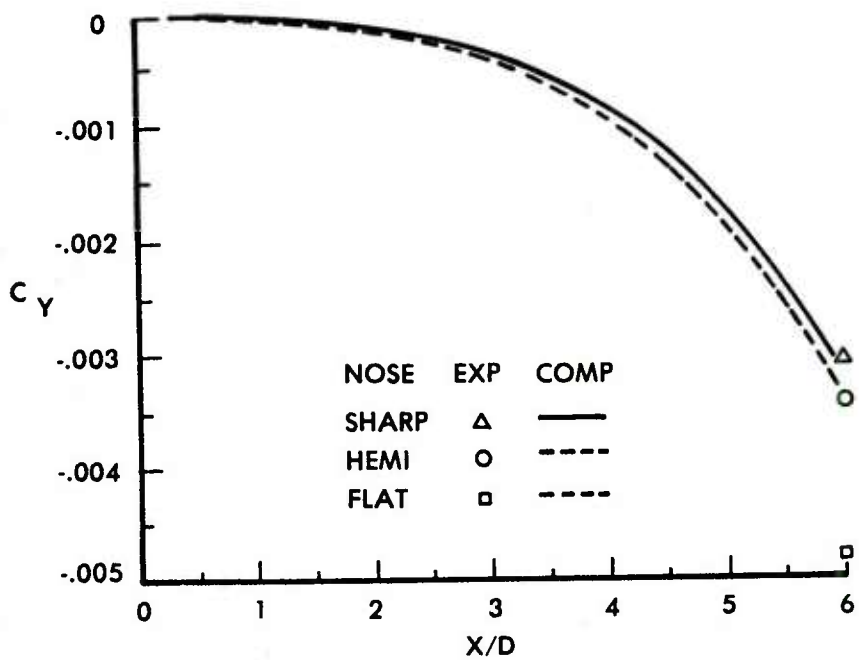

Figure 22. Magnus Force versus Axial Position, SOCBT Model, Computation Compared to Experimental Force Measurements, M = 3, $\alpha = 2°$, PD/V = 0.19, Wind Tunnel Test Conditions, Re = 9.19 $\times 10^6$/m

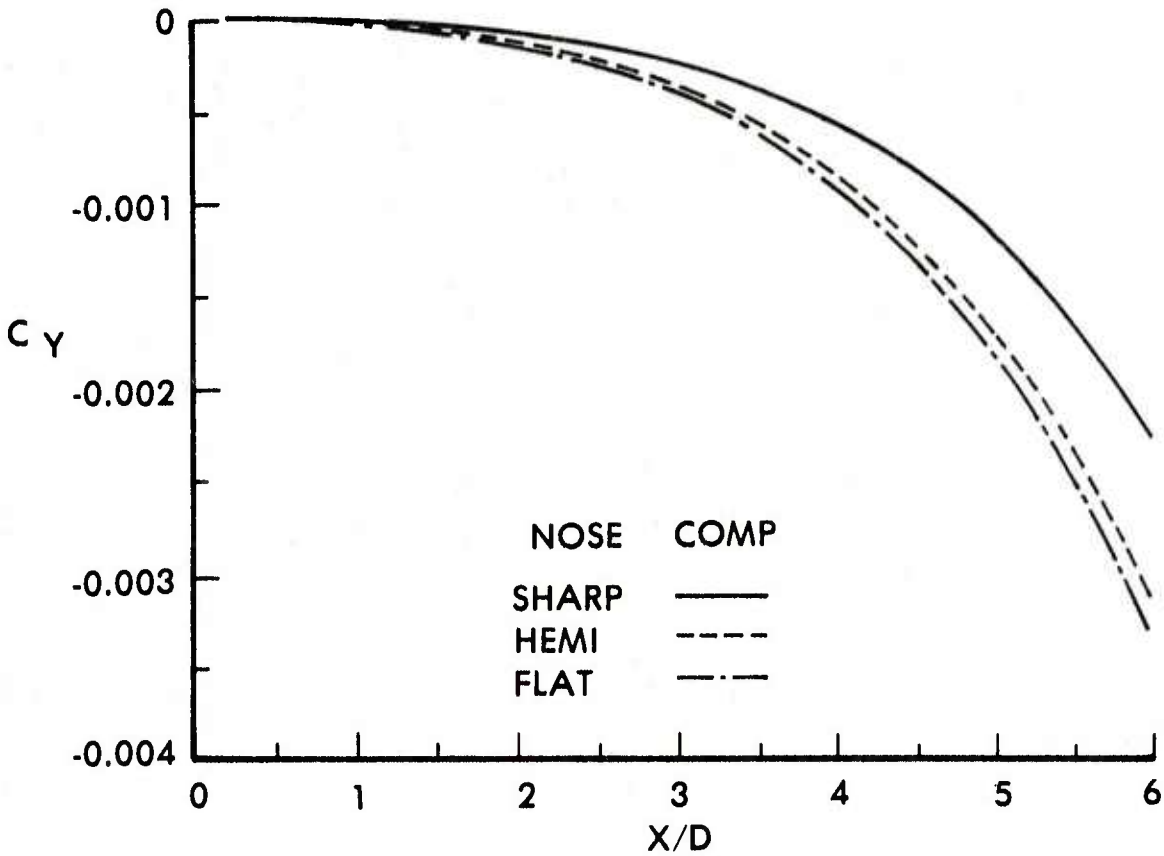

Figure 23. Magnus Force versus Axial Position, SOCBT Model, M = 3, α = 2°, PD/V = 0.19, Atmospheric Flight Conditions, Re = 6.80 $\times 10^7$/m

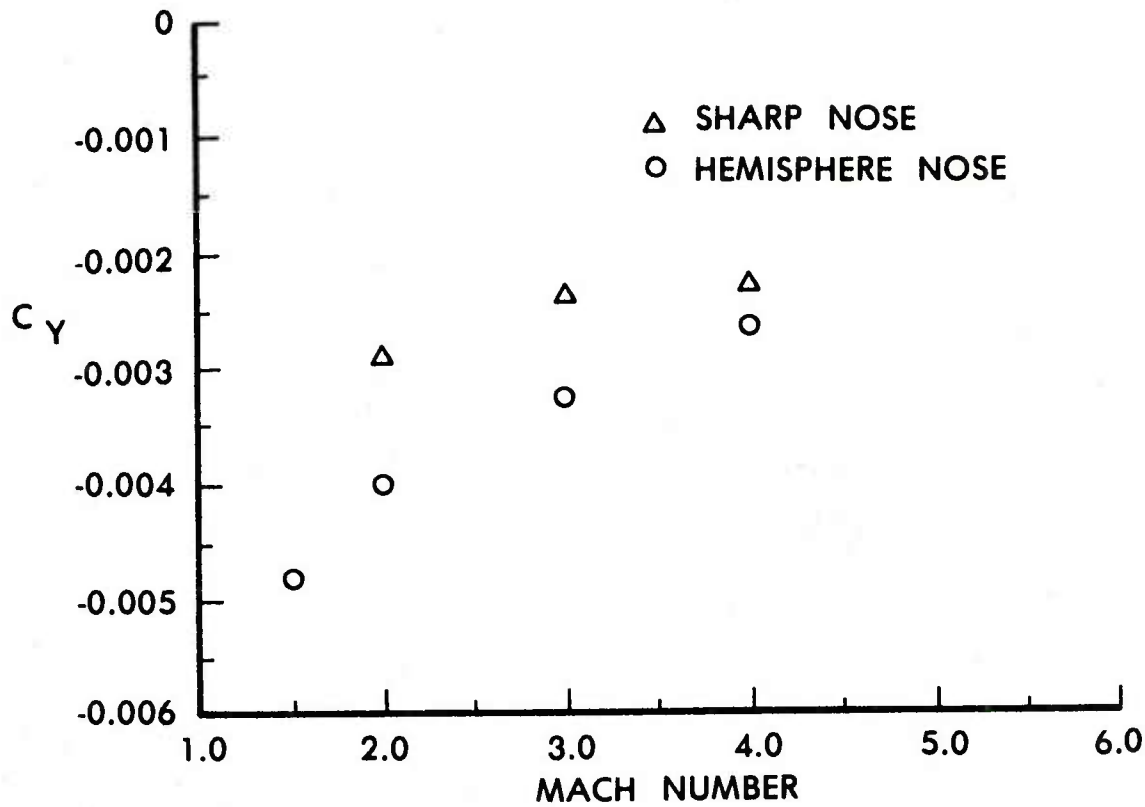

Figure 24. Magnus Force versus Mach Number, SOCBT Model, Comparison between Sharp and Hemisphere Noses, $\alpha = 2°$, PD/V = 0.19, Atmospheric Flight Conditions

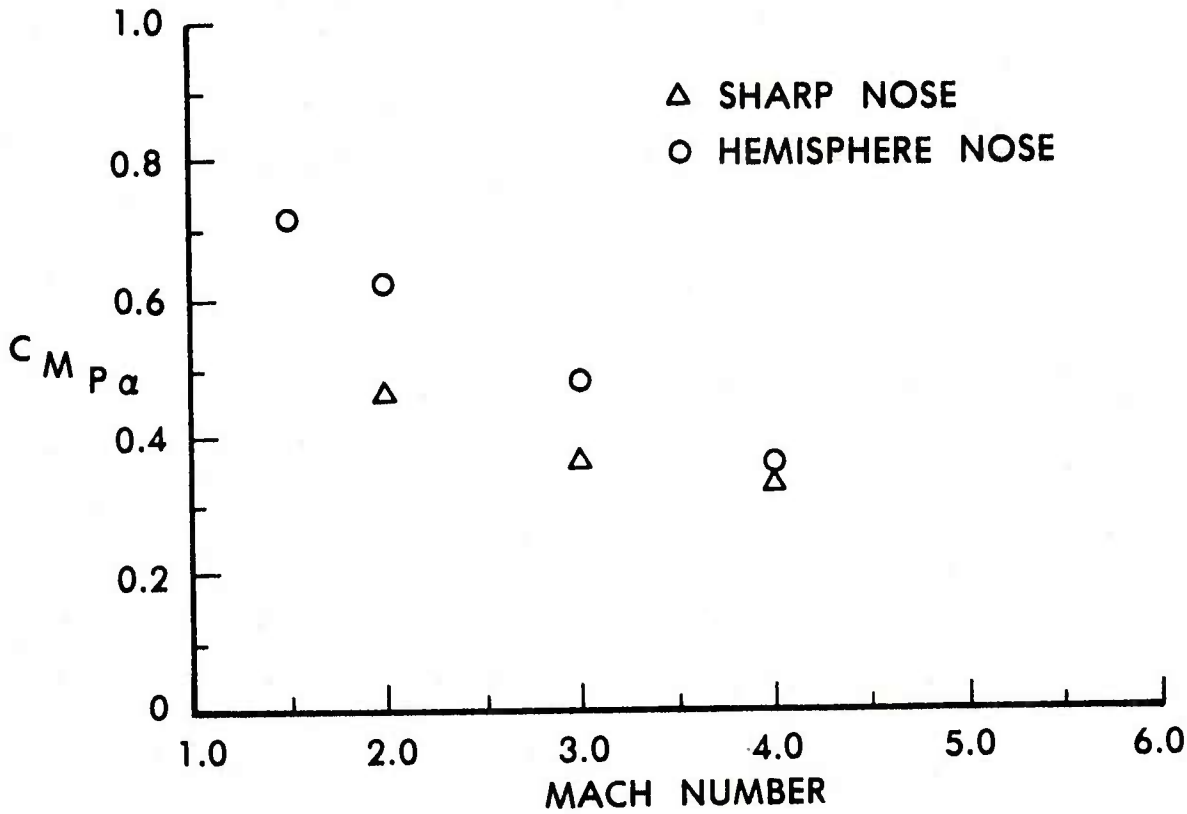

Figure 25. Slope of Magnus Moment Coefficient versus Mach Number, SOCBT Model, Comparison between Sharp and Hemisphere Noses, Atmospheric Flight Conditions

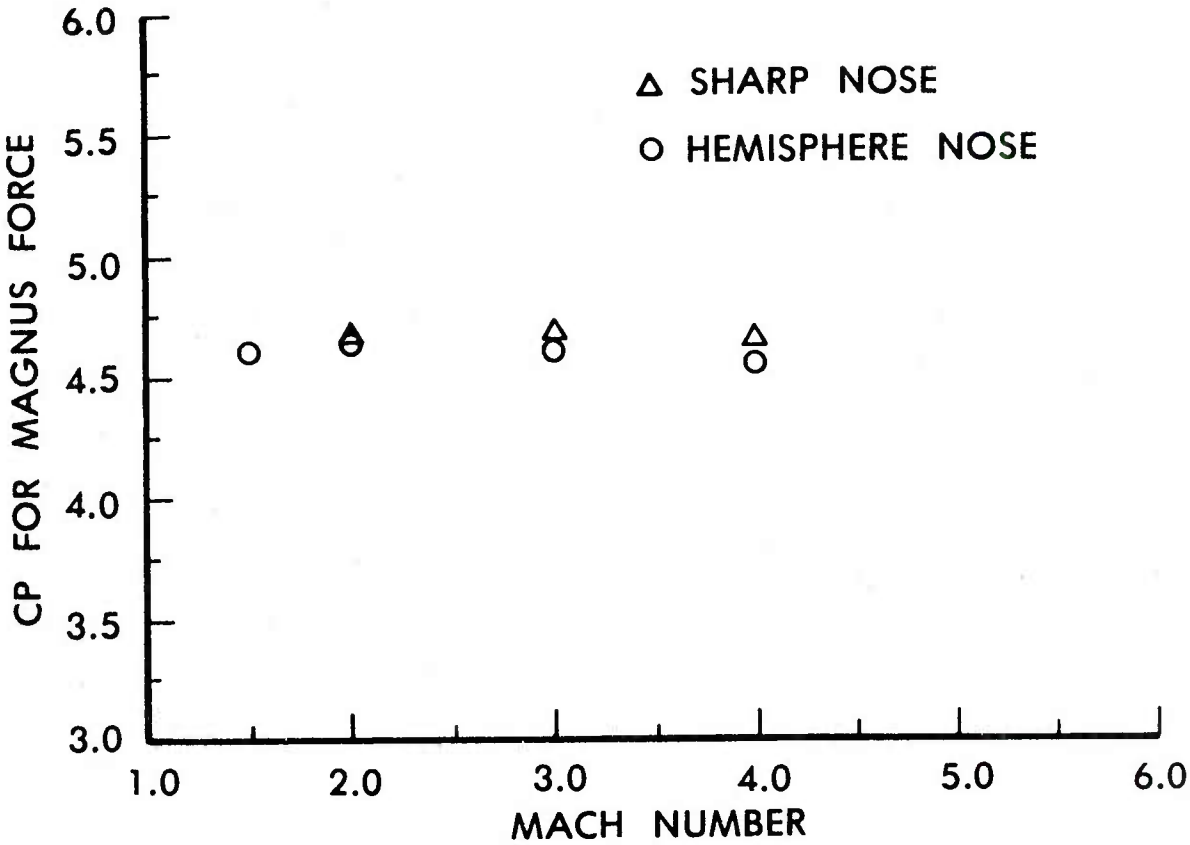

Figure 26. Magnus Force Center of Pressure versus Mach Number, SOCBT Model, Comparison between Sharp and Hemisphere Noses, Atmospheric Flight Conditions

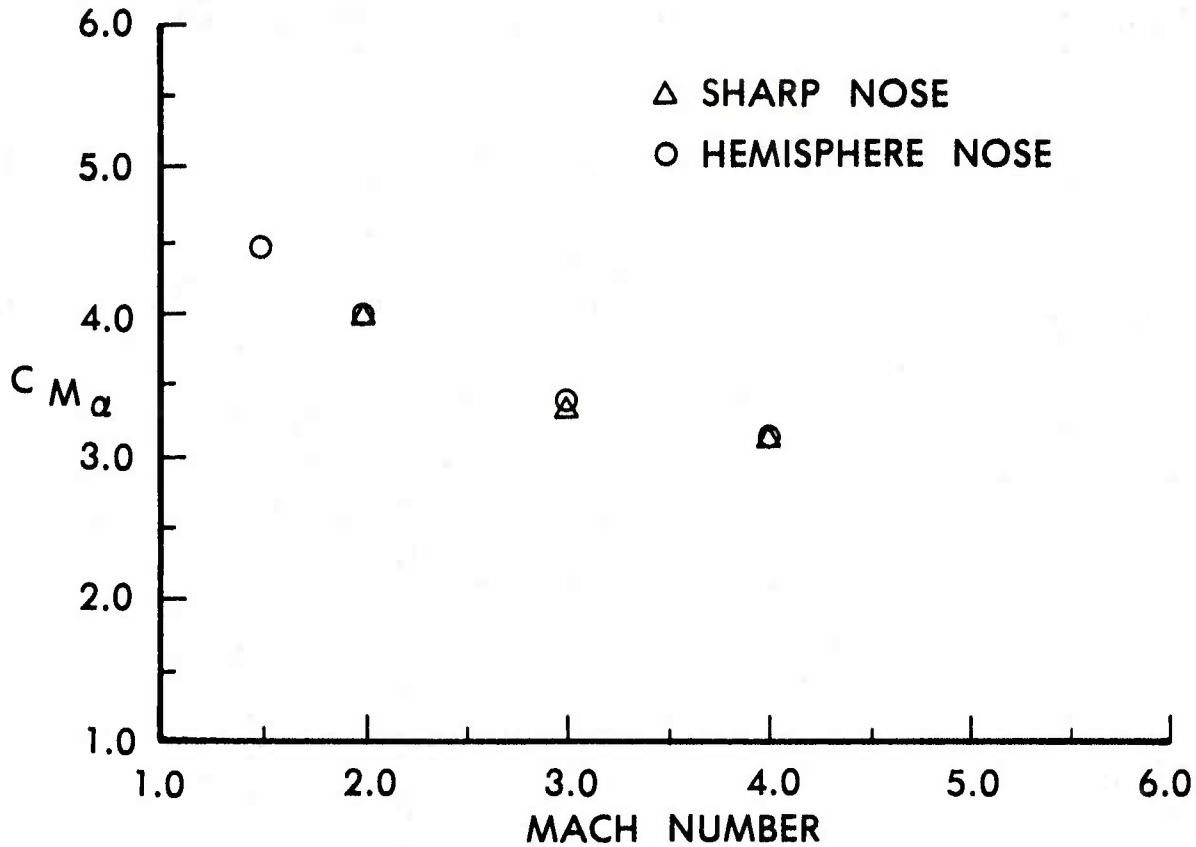

Figure 27. Slope of Pitching Moment Coefficient versus Mach Number, SOCBT Model, Comparison between Sharp and Hemisphere Noses, Atmospheric Flight Conditions

REFERENCES

1. Schiff, L.B., and Steger, J.L., "Numerical Simulation of Steady Supersonic Viscous Flow," AIAA Journal, Vol. 18, No. 12, December 1980, pp. 1421-1430.

2. Schiff, L.B., and Sturek, W.B., "Numerical Simulation of Steady Supersonic Flow Over an Ogive-Cylinder-Boattail Body," AIAA Paper No. 80-0066, AIAA 18th Aerospace Sciences Meeting, January 1980.

3. Sturek, W.B., and Schiff, L.B., "Computations of the Magnus Effect for Slender Bodies in Supersonic Flow," AIAA Paper No. 80-1586-CP, AIAA Atmospheric Flight Mechanics Conference, August 1980.

4. Baldwin, B.S., and Lomax, H., "Thin Layer Approximation and Algebraic Model for Separated Turbulent Flows," AIAA Paper No. 78-257, 1978.

5. Chaussee, D.S., Kutler, P., and Pulliam, T.H., "Three Dimensional Viscous Flow Field Program; Part I: Viscous Blunt Body Program (Interim Report)," AFWL-TM-81-63-FIMG, March 1981.

6. Nietubicz, C.J., and Opalka, K., "Supersonic Wind Tunnel Measurements of Static and Magnus Aerodynamic Coefficients for Projectile Shapes with Tangent and Secant Ogive Noses," ARBRL-MR-02991, U.S. Army Ballistic Research Laboratory/ARRADCOM, Aberdeen Proving Ground, MD 21005, February 1980 (AD A083297).

7. Unpublished Wind Tunnel Data. Test performed at the Naval Surface Weapons Center, White Oak Laboratory, Silver Spring, Maryland, for the U.S. Army Ballistic Research Laboratory.

LIST OF SYMBOLS

a	= speed of sound
CP	= center of pressure for normal force
CPY	= center of pressure for Magnus force
C_M	= pitching moment coefficient
$C_{M_{p\alpha}}$	= $d^2C_n/[d(\frac{PD}{V})\cdot d\alpha]$, slope of Magnus moment coefficient evaluated at $PD/V = 0$, $\alpha = 0$
C_n	= Magnus (yawing) moment coefficient
C_N	= normal force coefficient
C_Y	= Magnus (side) force
D	= diameter of model
e	= total energy per unit volume of fluid, normalized by $\rho_\infty a_\infty^2$
$\hat{E},\hat{E}_s,\hat{F},\hat{G}$	= flux vectors of transformed gasdynamic equation
J	= Jacobian of transformation between physical and computational coordinates
L	= reference length
M	= Mach number
p	= pressure normalized by $\rho_\infty a_\infty^2$
Pr	= Prandtl number, $\mu_\infty c_p/\kappa_\infty$
PD/V	= nondimensional spin rate about model axis
Re	= Reynolds number, $\rho_\infty U_\infty L/\mu_\infty$
$\hat{S}$	= viscous flux vector
u,v,w	= Cartesian velocity components along the x, y, z axis, respectively, normalized by a_∞
U,V,W	= contravariant velocity components
x,y,z	= physical Cartesian coordinate axes
α	= angle of attack
γ	= ratio of specific heats

LIST OF SYMBOLS (Cont'd)

κ = coefficient of thermal conductivity, normalized by free-stream value κ_∞

μ = coefficient of viscosity, normalized by free-stream value μ_∞

ξ, η, ζ = computational coordinates in the axial, circumferential, and radial directions (Fig. 1)

ρ = density, normalized by free-stream density ρ_∞

Subscripts

∞ = free-stream conditions

aw = adiabatic wall

w = body surface values

x = based on axial distance from nose

DISTRIBUTION LIST

No. of Copies	Organization
12	Administrator Defense Technical Info Center ATTN: DTIC-DDA Cameron Station Alexandria, VA 22314
1	Commander US Army Materiel Development and Readiness Command ATTN: DRCDMD-ST 5001 Eisenhower Avenue Alexandria, VA 22333
10	Commander US Army Armament Research and Development Command ATTN: DRDAR-TDC DRDAR-TSS DRDAR-LCA-F Mr. D. Mertz Mr. E. Falkowski Mr. A. Loeb Mr. R. Kline Mr. S. Kahn Mr. S. Wasserman Mr. H. Hudgins Dover, NJ 07801
1	Commander US Army Armament Materiel Readiness Command ATTN: DRSAR-LEP-L Rock Island, IL 61299
1	Director US Army Armament Research and Development Command Benet Weapons Laboratory ATTN: DRDAR-LCB-TL Watervliet, NY 12189
1	Commander US Army Aviation Research and Development Command ATTN: DRDAV-E 4300 Goodfellow Blvd. St. Louis, MO 63120
1	Director US Army Air Mobility Research and Development Laboratory Ames Research Center Moffett Field, CA 94035
1	Commander US Army Communications Rsch and Development Command ATTN: DRSEL-ATDD Fort Monmouth, NJ 07703
1	Commander US Army Electronics Research and Development Command Technical Support Activity ATTN: DELSD-L Fort Monmouth, NJ 07703
2	Commander US Army Missile Command ATTN: DRSMI-R DRSMI-RDK Mr. R. Deep Redstone Arsenal, AL 35898
1	Commander US Army Missile Command ATTN: DRSMI-YDL Redstone Arsenal, AL 35898
1	Commander US Army Tank Automotive Command ATTN: DRSTA-TSL Warren, MI 48090
1	Director US Army TRADOC Systems Analysis Activity ATTN: ATAA-SL White Sands Missile Range NM 88002
1	Commander US Army Research Office P. O. Box 12211 Research Triangle Park NC 27709

DISTRIBUTION LIST

No. of Copies	Organization
1	Commander US Naval Air Systems Command ATTN: AIR-604 Washington, D. C. 20360
2	Commander David W. Taylor Naval Ship Research and Development Center ATTN: Dr. S. de los Santos Mr. Stanley Gottlieb Bethesda, Maryland 20084
4	Commander US Naval Surface Weapons Center ATTN: Dr. T. Clare, Code DK20 Mr. P. Daniels Mr. D. A. Jones III Mr. L. Mason Dahlgren, VA 22448
2	Commander US Naval Surface Weapons Center ATTN: Code 312 Dr. C. Hsieh Dr. T. Zien Silver Spring, MD 20910
1	Commander US Naval Weapons Center ATTN: Code 3431, Tech Lib China Lake, CA 93555
1	Director NASA Langley Research Center ATTN: NS-185, Tech Lib Langley Station Hampton, VA 23365
2	Commandant US Army Infantry School ATTN: ATSH-CD-CSO-OR Fort Benning, GA 31905

No. of Copies	Organization
1	ACUREX Corporation/Aerotherm ATTN: Dr. M. J. Abbett 485 Clyde Avenue Mountain View, CA 94042
1	AVCO Corporation Research-Advanced Development Division 201 Lowell Street Wilmington, MA 01887
1	Nielsen Engineering & Research, Inc. ATTN: Dr. S. Stahara 510 Clyde Avenue Mountain View, CA 94043
2	Sandia Laboratories ATTN: Technical Staff, Dr. W.L. Oberkampf Aeroballistics Division 5631, H.R. Vaughn Albuquerque, NM 87115
1	Massachusetts Institute of Technology ATTN: Tech Library 77 Massachusetts Avenue Cambridge, MA 02139
1	University of Delaware Mechanical and Aerospace Engineering Department ATTN: Dr. J. E. Danberg Newark, DE 19711

Aberdeen Proving Ground

Dir, USAMSAA
ATTN: DRXSY-D
DRXSY-MP, H. Cohen

Cdr, USATECOM
ATTN: DRSTE-TO-F

Dir, USACSL, Bldg. E3516, EA
ATTN: DRDAR-CLB-PA
DRDAR-CLN
DRDAR-CLJ-L

USER EVALUATION OF REPORT

Please take a few minutes to answer the questions below; tear out this sheet, fold as indicated, staple or tape closed, and place in the mail. Your comments will provide us with information for improving future reports.

1. BRL Report Number _____

2. Does this report satisfy a need? (Comment on purpose, related project, or other area of interest for which report will be used.)

_____

_____

_____

3. How, specifically, is the report being used? (Information source, design data or procedure, management procedure, source of ideas, etc.) _____

_____

_____

4. Has the information in this report led to any quantitative savings as far as man-hours/contract dollars saved, operating costs avoided, efficiencies achieved, etc.? If so, please elaborate.

_____

_____

5. General Comments (Indicate what you think should be changed to make this report and future reports of this type more responsive to your needs, more usable, improve readability, etc.) _____

_____

_____

_____

6. If you would like to be contacted by the personnel who prepared this report to raise specific questions or discuss the topic, please fill in the following information.

Name: _____

Telephone Number: _____

Organization Address: _____

_____

_____